

Tropopause Folding Events to the East of Tibetan Plateau in Boreal Summer and their Remote Relation to the Circulation Anomalies over Northeastern Atlantic

Chuangdong Zhu (✉ zcd@lasg.iap.ac.cn)

Institute of Atmospheric Physics Chinese Academy of Sciences <https://orcid.org/0000-0002-8302-9444>

Rongcai Ren

Institute of Atmospheric Physics Chinese Academy of Sciences

Research Article

Keywords: Tropopause folding to the east of Tibetan Plateau, Circulation and weather, South Asian high, Rossby wave train

Posted Date: May 10th, 2021

DOI: <https://doi.org/10.21203/rs.3.rs-231772/v1>

License: © ⓘ This work is licensed under a Creative Commons Attribution 4.0 International License.

[Read Full License](#)

1 **Tropopause folding events to the east of Tibetan Plateau in boreal**
2 **summer and their remote relation to the circulation anomalies over**
3 **northeastern Atlantic**

4 Chuangdong Zhu^{1,3} and Rongcai Ren^{1,2*}

5 ¹*State Key Laboratory of Numerical Modeling for Atmospheric Sciences and*
6 *Geophysical Fluid Dynamics, Institute of Atmospheric Physics, Chinese Academy of*
7 *Sciences, Beijing 100029, China*

8 ²*Collaborative Innovation Center on Forecast and Evaluation of Meteorological*
9 *Disasters and KLME, Nanjing University of Information Science and Technology,*
10 *Nanjing 210044, China*

11 ³*Hubei Meteorological Service Center, Wuhan 430205, China*

12

13 ***Corresponding author:** Rongcai REN, LASG, Institute of Atmospheric Physics,
14 Chinese Academy of Sciences. E-mail: rrc@lasg.iap.ac.cn

15

16 **Abstract**

17 This study investigates the occurrence of tropopause folding (TF) events to the
18 east of Tibetan Plateau (ETP) (TF–ETP) in boreal summer. Firstly, it is revealed that,
19 anomalously frequent TF–ETP occurrence in summer, always corresponds to a
20 significant dipole rainfall anomaly pattern over China, with negative rainfall
21 anomalies over the upper and middle reaches of the Yangtze and Yellow river valleys,
22 and positive rainfall anomalies over eastern China. Secondly, the South Asian High
23 (SAH) center over Tibetan Plateau (TP) is found to be anomalously stronger when
24 occurrence of TF–ETP events is frequent. Further diagnosis indicates that, the
25 TF–ETP occurrence is related to an eastward propagating Rossby wave train (RWT)
26 that originates from a barotropic low anomaly center over the northeastern Atlantic
27 (NEA) about one–week before. The RWT propagates downstream via Western
28 Europe, the west of Baikal and down to East Asia along the mid-latitude westerlies,
29 and is connected to a high anomaly center over the north rim of TP, which enhances
30 the SAH center over TP. The enhanced SAH in turn favors the southward and
31 downward PV intrusion and the subsequent occurrence of TF–ETP. Furthermore, the
32 low anomaly center that initiates the RWT is related to dynamical forcing of transient
33 eddy activity over the NEA, which induces the low via eddy-forced upper divergence
34 and its pumping. Finally, such local and remote processes are confirmed in a typical
35 TF–ETP case. The ERA–Interim daily fields during 1979–2018 is used.

36 **Key words:** Tropopause folding to the east of Tibetan Plateau, Circulation and
37 weather, South Asian high, Rossby wave train.

38 1. Introduction

39 Tropopause folding (TF), or drastic deformation of the tropopause, is one of the
40 important stratosphere–troposphere interaction processes, and has been known to be
41 crucial for regional circulation and weather anomalies in the troposphere (Hoskins et
42 al. 1985; Holton et al. 1995; Tyrlis et al. 2013, 2014; Škerlak et al. 2014, 2015;
43 Akritidis et al. 2016, 2019; Vaughan et al. 2017; Dafka et al. 2020). TF was first
44 recognized in 1930s, when multiple stable stratification of temperature was detected
45 in the vertical direction from radio soundings. A conceptual TF model was then put
46 forward to explain such observational phenomenon and to understand the dynamical
47 mechanisms behind (Bjerknes and Palmén 1937). Because of the sharp increase in
48 potential vorticity (PV) from the troposphere to stratosphere, the tropopause in the
49 extratropics can also be represented by the 2 PVU surface ($1 \text{ PVU} = 10^{-6} \text{ m}^2 \text{ s}^{-1} \text{ K}$
50 kg^{-1}) (Ertel 1942; Reed 1955; Hoskins et al. 1985; Holton et al. 1995). Based on this,
51 TF events were also defined when multiple tropopause (i.e., the dynamical 2 PVU
52 surface) are detected in the vertical direction (Sprenger et al. 2003), which mostly
53 manifests a downward PV intrusion from the stratosphere (e.g., Hoskins et al. 1985).
54 TF events can be classified into three types based on the vertical span of them:
55 namely the vertically shallow, the medium and the deep ones (Sprenger et al. 2003).
56 When a TF event occurs, the downward intrusion of high PV air from the stratosphere
57 can result in significantly upper–level positive PV anomalies (e.g., Hoskins et al. 1985;
58 Tyrlis et al. 2013; Akritidis et al. 2016). The upper–level positive PV perturbations
59 can induce upward/downward air motion in the middle and lower troposphere

60 downstream/upstream of the perturbations (Hoskins et al. 1985, 2003), and thus
61 promote the development of deep convection due to the reduced static stability
62 beneath the positive PV perturbations (Morcrette et al. 2007; Russell et al. 2012). In
63 addition, interactions between such upper-level PV perturbations and the circulation
64 in the lower troposphere may also lead to rapid cyclogenesis in the lower troposphere
65 (e.g., Uccellini 1990; Browning and Golding 1995; Wernli et al. 2002), which is
66 usually accompanied with surface wind gust, extreme precipitation and other severe
67 weather anomalies in the lower troposphere (e.g., Goering et al. 2001; Antonescu et al.
68 2013; Kim et al. 2013; Škerlak et al. 2015). Nevertheless, intensity of the TF-related
69 circulation and weather anomalies are largely associated with the vertical span of the
70 TFs. Vertically deep and moderately deep TFs usually result in surface wind gust and
71 rainfall extremes, while vertically shallow TFs can induce relatively weaker rainfall
72 anomalies (Škerlak et al. 2014).

73 Most deep TFs, though being much less frequent ($< 0.1\%$) than shallow TFs (up
74 to 15%), occur mostly in winter because of the much stronger upper tropospheric
75 frontogenesis along the subtropical westerly jet (SWJ) located around 30°N (Škerlak
76 et al. 2015). They are often observed in the region from North America continent to
77 North Atlantic along the SWJ over there (Elbern et al. 1998; Sprenger et al. 2003;
78 Schmidt et al. 2006; Škerlak et al. 2015). Other TFs in winter, especially those often
79 observed in a zonally elongated region from the southeastern edge of Tibetan Plateau
80 (TP) to the south of Japan, are mostly shallow (Sprenger et al. 2003; Škerlak et al.
81 2015). In summer, vertically deep TFs are rarely observed due to the relatively much

82 weaker frontogenesis along the much weaker SWJ. The TFs frequently occurring
83 along the SWJ across the Eurasian continent are also mainly shallow (Tyrlis et al.
84 2014; Škerlak et al. 2015). Based on the summertime climatology of the TF frequency,
85 two hot spots are identified respectively over the eastern Mediterranean region and
86 over the central Asian region (Sprenger et al. 2003; Sprenger et al. 2003; Tyrlis et al.
87 2014; Škerlak et al. 2014, 2015), which coincide with two entrance regions of the
88 SWJ core centers (Sawyer 1956; Elbern et al. 1998; Sorensen and Nielsen 2001).
89 They were also related to dynamical interactions between the SAH and the SWJ
90 (Traub and Lelieveld 2003). At the western flank of the SAH, convergent southerlies
91 prevail in the upper troposphere over the eastern Mediterranean and central Asian
92 regions, which help to accelerate the SWJ and enhance the local vertical wind shear,
93 thus favoring the formation of a jet streak and TF occurrence there (Traub and
94 Lelieveld 2003). In agreement with this, recent studies indicated a possible linkage
95 between the TFs over these two hot spots with the Asian summer monsoon (Tyrlis et
96 al. 2014; Wu et al. 2018). It was found that TFs tend to occur at the northwestern side
97 of the monsoon-related upper-level anticyclone (i.e., the SAH), and become more
98 frequent when the monsoon SAH intensifies (Tyrlis et al. 2014; Wu et al. 2018).

99 On average, TP is a negative PV source for the upper atmosphere because of its
100 powerful thermal forcing in summer, which is highly responsible for the existence of
101 the giant SAH system (Wu and Liu 2000; Liu et al. 2001). In pace with the variation
102 of TP thermal forcing, the intensity as well as the zonal location of the SAH center
103 oscillates eastward and westward periodically in seasonal and sub-seasonal timescale

104 (Ren et al. 2015; Yang and Li 2016; Ren et al. 2019). Diagnosis of the total PV fields
105 during SAH oscillations demonstrated that the zonal oscillation of the SAH center is
106 accompanied by periodic southward and westward eddy shedding around the eastern
107 and southeastern edge of the SAH (Hsu and Plumb 2000; Popovic and Plumb 2001;
108 Liu et al. 2007; Vogel et al. 2014; Ortega et al. 2017). Particularly, the southward eddy
109 shedding can result in filament-like high PV center to the east of SAH (Vogel et al.
110 2014; Ortega et al. 2017). Meanwhile, the powerful TP thermal forcing also results in
111 a radical downward concave of isentropic surfaces, but a radical uplift of PV surfaces
112 as well as the tropopause over TP. The isentropic surfaces and PV surfaces (or the
113 tropopause) may intersect almost orthogonally over the surrounding region of TP
114 (Ren et al. 2014; Xia et al. 2016). This gives rise to southward and downward high PV
115 intrusion along isentropic surfaces from the extratropical stratosphere into the lower
116 latitude troposphere over the ETP region (Ren et al. 2014; Xia et al. 2016), and thus
117 favors the TF-ETP occurrence there in summer. Tyrlis et al. (2013) also suggested
118 that upper-level northerlies and accompanied subsidence are favorable large-scale
119 conditions for the occurrence of TF-ETP.

120 The occurrence of TF-ETP, though much less frequent than the TFs over the two
121 hot spots (Tyrlis et al. 2013, 2014; Škerlak et al. 2014, 2015), is closely related with
122 the circulation and weather anomalies over East Asia and China. Previous studies
123 indicated that the high PV air near the tropopause can penetrate into the troposphere
124 during TF-ETP events in summer, favoring the development of strong convection and
125 heavy precipitation over East Asia (Liu and Li 2010; Shou et al. 2014; Cui et al. 2016;

126 Zhao and Yao 2017). However, most of the evidence of TF–ETP occurrence and its
127 impacts are mostly based on scatted case studies. With the much–extended time series
128 of related meteorological data fields, a more comprehensive investigation is still lack,
129 which has obviously hindered our further understanding of the thermodynamic
130 processes related to TF–ETP occurrence and its general climate impacts. By using the
131 currently available longer time series provided by ERA–Interim, this study is aimed to
132 perform a more comprehensive investigation on TP–ETP events and provide a much
133 general picture of the impacts of TF–ETP occurrence on the tropospheric circulation
134 and weather anomalies over East Asia and China in summer. We will also explore the
135 relationship between the SAH and TF–ETP occurrence and the dynamical processes
136 linking the TF–ETP and the SAH. The results may advance our understanding of the
137 weather and climate anomalies in East Asia and China from a new perspective and
138 benefit the predictions of them.

139 This paper is organized as follows. Section 2 introduces the data and method;
140 Section 3 shows the occurrence of TF–ETP and its impacts on the surrounding
141 circulation and rainfall, demonstrates the association of TF–ETP occurrence with
142 SAH variability, and provides evidence of a remote linkage from TF–ETP to
143 circulation anomalies over the northeastern Atlantic (NEA) by the results of
144 composite and regressed analysis; Section 4 presents a typical TF–ETP case to verify
145 the displayed processes in section 3; Summary is provided in Section 5.

146 **2. Data and Method**

147 *2.1 Data*

148 The daily circulation fields from the ERA–Interim data set provided by the
149 European Center for Medium–Range Weather Forecasts (Dee et al. 2011) are used,
150 which cover the period 1979–2018, with a horizontal resolution of $1.5^\circ \times 1.5^\circ$ in
151 latitude and longitude and on 37 pressure levels spanning from 1000–hPa to 1–hPa in
152 the vertical direction. To diagnose TF events using isentropic circulation fields, we do
153 interpolation of circulation fields from the 37 isobaric surfaces onto 17 isentropic
154 surfaces spanning from 260K to 420K. The daily precipitation data on a horizontal
155 resolution of $0.5^\circ \times 0.5^\circ$ in latitude and longitude during 1979–2018 is obtained from
156 CPC Global Unified Precipitation Project (Chen et al. 2008). Daily anomaly fields are
157 obtained by removing the daily annual cycle of all the circulation fields. Regarding
158 that the meridional position of the SAH as well as the circulation pattern is relatively
159 stable during the boreal summertime, the period from July 1st to August 31st is mainly
160 concerned in this study.

161 2.2 Method

162 The 2 PVU surface ($1\text{PVU} = 10^{-6} \text{ m}^2 \text{ s}^{-1} \text{ K kg}^{-1}$) is widely used to represent the
163 dynamical tropopause (e.g., Hoskins et al. 1985; Holton et al. 1995). A TF is usually
164 defined at one grid point when multiple dynamical tropopause (2 PVU surface) can be
165 found in the vertical direction (Sprenger et al. 2003; Škerlak et al. 2014). Specifically,
166 with the occurrence of a TF at one grid point, three pressure surfaces (upper one: P_U ;
167 middle one: P_M ; lower one: P_L) that intersect with the tropopause can be detected. The
168 pressure difference between the middle and upper ($\Delta p = P_M - P_U$) is regarded as the
169 vertical extent of the TF. And TFs with $\Delta p \geq 350$ –hPa are defined as deep TFs, those

170 with $200 \leq \Delta p < 350$ -hPa are defined as medium TFs, and those with $50 \leq \Delta p <$
 171 200 -hPa are defined as shallow TFs, while those with $\Delta p < 50$ -hPa are not
 172 considered as TFs (Škerlak et al. 2014). As vast majority of TFs in summer are
 173 vertically shallow (Tyrlis et al. 2014; Škerlak et al. 2014, 2015), the TFs concerned in
 174 this study are all shallow TFs.

175 Firstly, we calculate the TF frequency at each grid point based on the daily
 176 binary (0: no folding; 1: folding) time series in the 40 summer seasons (July–August)
 177 from 1979 to 2018:

$$178 \quad f_{TF}(x, y) = \frac{\sum_{t=1}^{t=N} TF(t, x, y)}{N}, \quad (1)$$

179 where

$$180 \quad TF(t, x, y) = \begin{cases} 0, & \text{no folding} \\ 1, & \text{folding} \end{cases}, \quad (2)$$

181 (x, y) represents the horizontal position of the grid point, t is time, N is the sample size
 182 of the selected time series. Secondly, we define a TF–ETP index (TFI) by averaging
 183 the above–mentioned daily binary time series ($TF(t, x, y)$) over the area to the east of
 184 TP, to measure the TF occurrence over the area to the ETP region (33° – 45° N,
 185 105° – 117° E; red dash box in Fig. 1a) quantitatively. Subsequently, 438 cases of high
 186 TFI (i.e., TF–ETP is frequent) are identified with a threshold of 1 standard deviation
 187 of the TFI time series (shown in Fig. 1b). Moreover, a PV index (PVI) manifesting the
 188 downward intrusion of stratospheric PV is also defined by averaging the 300–hPa PV
 189 anomalies over the same area. The TFI as well as the PVI is used for the following
 190 investigation of TF–ETP.

191 To describe the Rossby wave propagation associated with TF–ETP, we diagnose
 192 the three–dimensional wave activity flux (F_s) defined by Plumb (1985):

$$193 \quad F_s = \frac{p \cos \phi}{p_0} \times \left(\begin{array}{c} v'^2 - \frac{1}{2\Omega a \sin 2\phi} \frac{\partial(v'\Phi')}{\partial \lambda} \\ -v'u' + \frac{1}{2\Omega a \sin 2\phi} \frac{\partial(u'\Phi')}{\partial \lambda} \\ \frac{2\Omega \sin \phi}{S} \left[v'T' - \frac{1}{2\Omega a \sin 2\phi} \frac{\partial(T'\Phi')}{\partial \lambda} \right] \end{array} \right), \quad (3)$$

194 where

$$195 \quad S = \frac{\partial \hat{T}}{\partial z} + H, \quad (4)$$

196 denotes the static stability (the caret means area–average over the region to the north
 197 of 20°N), ϕ and λ are latitude and longitude, u and v denote zonal wind and
 198 meridional wind, Φ refers to the geopotential height, T refers to the air temperature,
 199 a is Earth’s radius, and Ω is Earth’s rotational angular velocity. The prime represents
 200 deviation from zonal mean. As wave activity flux is parallel to the local group
 201 velocity of a Rossby wave, it can be used to denote the propagating direction of
 202 Rossby wave energy. To diagnose transient eddy activities associated with the
 203 development of RWT, we first extract synoptic-scale (2.5–6 days) transient eddy
 204 component (u', v') from the daily horizontal wind field using Lanczos band pass
 205 filter (Duchon 1979). We then calculate the transient eddy kinetic energy
 206 $(u'^2 + v'^2)/2$ in the upper troposphere at 300–hPa.

207 **3. Results from composite and regression**

208 *3.1 TF–ETP occurrence and its impacts in East Asia*

209 Firstly, we show the summertime (July–August) climatology of the TF frequency,
210 the SWJ and the SAH at 200–hPa in Fig. 1a. It is seen that TFs do mainly occur along
211 the SWJ that lies to the north edge of the SAH, and two major TF frequency centers
212 (up to 10% and 8%) are found respectively over the eastern Mediterranean and over
213 the central Asia region (Fig. 1a), as also indicated in previous studies (Tyrlis et al.
214 2014; Škerlak et al. 2015). These two centers are just at the upstream of two SWJ core
215 centers because of much stronger upper–level frontogenesis in the entrance region of
216 SWJ (Elbern et al. 1998; Sorensen and Nielsen 2001). It can also be seen from Fig. 1a
217 that, there exists a minor TF frequency center (up to 3%) over the east of TP, which
218 we will mainly concern because of the critical impacts of its variability on
219 tropospheric circulation and weather in East Asia and China, as will be shown in Fig.
220 3 below. Figure 1b displays the temporal evolution of the daily TFI or the day–to–day
221 variation of TF–ETP, which exhibits considerably strong pulse–like variability
222 accompanied with almost complete quietness in most of the summertime. Based on
223 the above definition, every TFI pulse basically indicates that TFs are occurring over a
224 considerable large area to the east of TP. Power spectral analysis of the daily TFI
225 reveals that the pulse–like variability in summer is dominated by a quasi–biweekly
226 period (about 13 days) (Fig. 1c). This implies that TF–ETP is indeed an atmospheric
227 phenomenon that occurs within the Asian summer monsoon system where
228 quasi–biweekly variability is recurrent during its mature phase (Krishnamurti and
229 Bhalme 1976; Krishnamurti and Ardanuy 1980; Ortega et al. 2017).

230 Taking unit standard deviation of the daily TFI time series as a threshold, Figs.

231 2a-b show vertical cross-sections of the composite PV and its anomalies along 39°N
232 and along 111°E, respectively. It is clear that summer climatology of 2 PVU surface
233 to the east of TP (i.e., the dynamical tropopause) is remarkably concave, manifesting
234 the effect of frequent TF occurrence there. As occurrence of TFs is accompanied with
235 downward and southward high PV intrusion from the stratosphere into the
236 tropospheric layer, significant positive PV anomalies can be induced in the upper
237 troposphere. From the PV perspective put forward by Hoskins et al. (1985, 2003),
238 upper-level positive PV anomalies can induce downward motion behind and upward
239 motion ahead, which can act to suppress and promote the local convective activities
240 respectively. As a result, cyclogenesis will be favored ahead of upper-level positive
241 PV anomalies (Hoskins et al. 1997). It is seen from Figs. 2a-b that, when TF-ETP is
242 frequent, the dynamical tropopause over the ETP region is even lower than its
243 climatology. And there do appear significant positive PV anomalies in the upper
244 troposphere over the ETP region (Figs. 2a, 2b and 3a). Meanwhile, significant
245 downward/upward motion anomalies do appear beneath and behind/ahead-of the
246 upper-level positive PV anomalies, which are accompanied by a prominent
247 convergence/divergence anomaly center in the upper troposphere (Figs. 2c-d).

248 In association with this, Eastern China is dominated by a cyclonic anomaly
249 center with significant convergence anomalies in the lower troposphere (Fig. 3b),
250 accompanied with positive rainfall anomalies (Fig. 3c). Meanwhile, significant
251 divergence anomalies accompanied with negative rainfall anomalies appear in the
252 upper and middle reaches of the Yangtze and Yellow river valleys, in association with

253 the anomalous northerlies prevailing behind the cyclonic anomaly center (Figs. 3b-c).
254 In general, frequent TF–ETP occurrence is related to a significant dipole rainfall
255 anomaly pattern over China, with negative rainfall anomalies in the upper and middle
256 reaches of the Yangtze and Yellow river valleys, and positive rainfall anomalies in
257 Eastern China.

258 *3.2 TF–ETP occurrence and SAH variability*

259 Figure 4 shows the composite distributions of TF frequency, the SAH and the
260 related SWJ at 200–hPa for high TFI days. As anticipated from the TFI definition, the
261 maximal frequency of TFs over the ETP region during high TFI days can be as high
262 as 10%, which is accompanied by an anomalously stronger SAH center over the TP
263 region compared with the summer climatology (Fig. 4 vs Fig. 1a). This suggests that
264 frequent TF activity over the east of TP is closely related to an anomalously stronger
265 SAH center over TP. The much stronger northerlies to the northeast of a stronger
266 SAH center may act to enhance the downward and southward PV intrusion that
267 induces TF activities (as will be shown in Fig. 5a). In addition, the TF activity over
268 the north of TP during high TFI days is also much active than that in the summer
269 climatology, which can be attributed to the stronger SWJ to the north of a relatively
270 stronger SAH center (Fig. 4 vs Fig. 1a). It should be noted that, the close relationship
271 between the TF–ETP occurrence and the SAH intensity over TP does not indicate a
272 direct relation between the TF–ETP occurrence and the quasi-biweekly east-west
273 oscillation of the SAH center. In fact, the correlation between the TF–ETP occurrence
274 and the quasi-biweekly east–west oscillation of the SAH center is just moderate and

275 statistically insignificant (not shown). This implies that the east–west oscillation of
276 the SAH center may not fully represent the intensity variation of the SAH over TP.

277 *3.3 A Rossby wave train (RWT) linking the TF–ETP occurrence to the NEA*

278 Shown in Fig. 5a are the composite meridional wind and vertical motion
279 anomalies at 200–hPa for high TFI days. Firstly, the significant northerly anomaly
280 center to the northeast of TP (Fig. 5a) is obviously related to an anomalously stronger
281 SAH center over TP (Fig. 5b). Associated with this are significant descent anomalies
282 to the northeast of TP (Fig. 5a), which may be a manifestation of the enhanced
283 TF–related downward and southward PV intrusion from the extratropical stratosphere.
284 Observing the successive positive and negative meridional wind anomaly centers
285 across Eurasian continent, a clear RWT pattern can be identified, which passes across
286 Western Europe, the western Russia, the northwest of Baikal, and the northeast of TP
287 and down to the east of Hetao Plain (Fig. 5a). Similar RWT pattern can be seen from
288 the composite geopotential height anomalies at 200–hPa, which is consisted of three
289 high anomaly centers respectively over Western Europe, the north rim of TP and the
290 Sea of Japan; and two low anomaly centers over the west of Baikal and the northeast
291 of TP (Fig. 5b). Existence of the RWT is confirmed by the composite wave activity
292 flux anomalies (Fig. 5b). It is seen that the RWT originates from Western Europe,
293 then propagates eastward along the north edge of the SWJ, and happens to shift
294 southeastward when it goes across the strongest core of the SWJ that is just to the
295 north of the SAH center (Fig. 5b) because of the Rossby wave–guide effect of the
296 SWJ (Hoskins and Ambrizzi 1993; Terao 1999).

297 Obviously, the RWT-related high anomaly center over the north rim of TP for
298 high TFI days, can help to intensify the SAH (Fig. 5b). The intensified SAH can in
299 turn, lead to anomalously strong northerlies, and thus descent anomalies over the
300 northeast of TP as shown in Fig. 5a, favoring the occurrence of TF-ETP. These
301 results suggest that the occurrence of TF-ETP may be remotely connected to the
302 circulation anomalies over Western Europe via this upper-level RWT.

303 As suggested by previous studies, TF activity is usually accompanied by
304 significant downward PV intrusion from the lower stratosphere to the upper
305 troposphere (e.g., Hoskins et al. 1985; Tyrlis et al. 2013; Akritidis et al. 2016).
306 TF-ETP events also correspond well to significant PV anomalies around 300-hPa
307 over the ETP region as shown in Fig. 3a. Next, we define a PV index (PVI) by
308 averaging the PV anomalies at 300-hPa over the ETP region, to obtain a much
309 smoother temporal evolution of the TF-ETP activities compared to the TFI. The PVI
310 is used below to further investigate the origin and evolution of the above-mentioned
311 RWT.

312 Figure 6 shows the lead/lag regressions of geopotential height, horizontal wave
313 activity flux anomalies, and vertical motion anomalies at 200-hPa against the PVI in
314 boreal summer. At day -7 (i.e., seven days before TF-ETP occurrence), an anomalous
315 low over the NEA begins to act as a source of Rossby wave. And a RWT is initiated,
316 propagating downstream, resulting in an anomalous high over Western Europe, an
317 anomalous low over the northeast of Mediterranean and an anomalous high over
318 Caspian Sea (Fig. 6a). The wave activity flux anomalies indicate a RWT pattern
319 connecting these anomaly centers.

320 Subsequently, with the downstream dispersion of Rossby wave energy along the
321 westerlies in the mid-latitudes, the three downstream anomaly centers along the RWT,
322 get intensified successively. Meanwhile, the initial low anomaly center over the NEA
323 region begins to get gradually weakened (Figs. 6a–d). During this period, the anomaly
324 centers also move eastward along the RWT. Till day –3, the RWT has propagated
325 further eastward along the SWJ to the east of TP as suggested by wave activity flux
326 anomalies (Fig. 6e). Correspondingly, new anomaly centers appear farther
327 downstream including a weak low anomaly center over the north of TP and a
328 relatively strong high anomaly center over the east of TP (Fig. 6e). Subsequently, the
329 RWT continues to propagate eastward, with gradual intensification and eastward
330 movement of those anomaly centers (except the high anomaly center over Western
331 Europe) (Figs. 6f–h). The low anomaly center from the NEA region, however,
332 gradually diminishes and nearly disappears till day –2 (Figs. 6e–f). Then a complete
333 RWT is consisted of three high anomaly centers respectively over Western Europe,
334 the north rim of TP and the Sea of Japan, and two low anomaly centers over the
335 region west of Baikal and northeast of TP (Fig. 6h). Accompanying the development
336 of the RWT, significant descent/ascent anomalies also become significant ahead of
337 the high/low anomaly centers along the RWT, especially the descent anomaly center
338 ahead of the high anomaly center over the northwestern TP (Fig. 6e). This descent
339 anomaly center is getting remarkably intensified while moving eastward (Figs. 6f–h).
340 It becomes the strongest when it arrives in the region to the northeast of TP (also the
341 northeast of the SAH) till day 0, which favors the occurrence of TF–ETP there (Fig.

342 6h). It should be noted that the RWT over Eurasian continent at day 0 highly
343 resembles that of the composite result against the TFI (Fig. 6h vs. Fig. 5b), confirming
344 again the robustness of the TF–ETP–related RWT as well as the reasonableness of our
345 choice to use the PVI to investigate the origin and evolution of the RWT.

346 To further demonstrate the occurrence of PV intrusion associated with TF–ETP,
347 we show in Fig. 7 the lead/lag regressions of PV, meridional PV advection (MPVA)
348 and meridional wind anomalies at 200–hPa against the PVI. Obviously, the RWT
349 pattern manifested by PV anomalies resembles that in Figs. 5–6. It extends from the
350 NEA to Caspian Sea region at day –7, consisted of two positive PV anomaly centers
351 respectively over the NEA and the north of Mediterranean, and two negative PV
352 anomaly centers respectively over Western Europe and Caspian Sea region (Fig. 7a).
353 From day –7 to day –4, while most of the downstream PV anomaly centers gradually
354 get intensified accompanying the eastward propagation of the RWT, the positive PV
355 anomaly center originally located over the NEA gradually get weakened (Figs. 7a–d).
356 When the RWT propagates downstream to the north of TP till day –4, a positive PV
357 anomaly center appears over there (Fig. 7d). Later, with the decaying of the initiated
358 positive PV anomaly over the NEA, the RWT pattern is clear over the region from
359 Western Europe to East China at day –2 (Fig. 7f). Till day 0 when TF–ETP occurs,
360 the RWT has propagated downstream to the Sea of Japan, with remarkably intensified
361 positive PV anomalies respectively over the west of Baikal and northeast of TP and
362 negative PV anomalies respectively over the north rim of TP and the Sea of Japan
363 (Fig. 7h). It should be noted that, ahead of the negative PV anomaly center over the

364 north rim of TP, there do exist significant northerly and positive MPVA anomalies,
365 which favor the occurrence of TF–ETP (Fig. 7h).

366 *3.4 Origin of the low anomaly center over the NEA*

367 We know from above that, the TF–ETP–related RWT is initiated from a low
368 anomaly center over the NEA (i.e., the northeastern Atlantic). In this section, we
369 further investigate the possible origin of this low anomaly center over the NEA.
370 Previous studies indicated that the North Atlantic, located at the exit region of the
371 North American SWJ, is one of the most active regions with synoptic-scale transient
372 eddy activities which can excite low-frequency circulation anomalies (Blackmon,
373 1976; Holopainen et al. 1982) and are maintained by recurrent barotropic energy
374 conversion from the background flow (Xu et al. 2019). We show in Fig. 8a the lead
375 regressions of transient eddy kinetic energy anomalies at 300–hPa against the PVI.
376 Since day –9 before TF–ETP occurrence, there appear positive anomalies of transient
377 eddy kinetic energy over the NEA, which are gradually enhanced and become the
378 strongest at day –7, indicating anomalously stronger transient eddy activities over the
379 NEA before the TF–ETP occurrence. It is also seen from Fig. 8a that the anomalously
380 stronger transient eddy activities are accompanied by positive vorticity advection
381 anomalies over the NEA, which manifest the dynamical effect of anomalously
382 stronger transient eddy activities. Previous studies also suggested that synoptic-scale
383 transient eddy activities can lead to low-frequency circulation anomalies by inducing
384 eddy vorticity (Lau and Holopainen, 1984; Mullen, 1987; Lau and Nath, 1991). Fig.
385 8b shows the spatial pattern of the transient eddy kinetic energy and vorticity

386 advection anomalies at day -7 , and location of the westerly jet in boreal summer. It is
387 seen that active transient eddy activities are located at the right side of the exit region
388 of the North American SWJ, accompanied by a vorticity advection anomaly center.

389 To further demonstrate the dynamical processes via which the NEA low anomaly
390 center is excited, we display in Figs. 9a–b the vertical cross-sections of the regressed
391 circulation anomalies over the NEA at day -7 . It is seen that, associated with the
392 anomalously strong transient eddy forcing and positive vorticity advection, there exist
393 low-frequency divergence anomalies over the NEA in the upper troposphere, which
394 are synchronized with dynamical ascent and convergence anomalies in the lower
395 troposphere due to the dynamical pumping effect of the upper divergence. The lower
396 convergence anomalies in turn are related with positive vorticity (or cyclonic)
397 anomalies in the lower troposphere. This explains the vertically barotropic structure of
398 the low anomaly center over the NEA (Fig. 9a). The dynamical nature of this low
399 anomaly center can also be seen clearly from the same barotropic structure of
400 geopotential height anomalies, which is corresponded with cold anomalies in the
401 troposphere below 250-hPa due to the adiabatic cooling caused by the dynamical
402 ascent anomalies (Fig. 9b). Therefore, it is the dynamical forcing of the anomalously
403 stronger transient eddy activities that has excited the NEA low anomaly center that
404 initiates the RWT propagating downstream to East Asia. Consistent with this,
405 previous studies also showed that cyclone activities are indeed active over the North
406 Atlantic stretching from the east coast of America to the west coast of Western Europe
407 (Sanders et al. 1980; Allen et al. 2010), and those originated in the eastern North

408 Atlantic are characterized with barotropic structure (Lau, 1979; Hoskins and Valdes,
409 1990).

410 To summarize, the TF–ETP occurrence, though relatively less frequent than the
411 two hot-spots of TFs respectively over the eastern Mediterranean region and over the
412 central Asian region, has significant impacts on the rainfall anomaly pattern over East
413 Asia; It is remotely connected to the transient eddy forcing anomalies over the NEA
414 region via a RWT that successively propagates eastward to East Asia. The RWT
415 connects to a high anomaly center over the north rim of TP, which helps to enhance
416 the SAH center over TP. The enhanced SAH center can then induce anomalously
417 stronger northerlies and subsidence motion, and consequently contribute to stronger
418 southward and downward PV intrusion over the northeast of TP, which favors the
419 occurrence of TF–ETP.

420 **4. A typical TF–ETP case in 1990**

421 To verify the composite and regressed results in the above section, next we
422 choose a typical TF–ETP event occurred on 3 August 1990. Firstly, it is seen from Fig.
423 10a that, there exist strong PV anomalies in the upper troposphere over the ETP
424 region associated with the strong southward and downward PV intrusion during this
425 TF–ETP event (Figs. 11a-b). In association with this, large amount of rainfall can be
426 observed in Eastern China and less amount of rainfall in the upper and middle reaches
427 of the Yangtze and Yellow river valleys (Fig. 10b). Particularly, it can be seen that
428 this anomalous dipole pattern of rainfall over China is related to the strong
429 descent–ascent anomaly pattern in the mid-troposphere from the descent region

430 behind, to the ascent region ahead of the PV anomaly center in the upper layer (Figs.
431 11c-d).

432 In Figure 12, we display the synchronized evolution of the tropopause and its
433 folding locations, the SAH at 200-hPa, and the PV and meridional wind anomalies at
434 350K isentropic surface. On 26 July, positive PV anomalies appear over the NEA (Fig.
435 12a), resembling to the regressed results shown in Fig. 7a. Southeastward downstream
436 are negative, positive, and negative PV anomalies prevailing respectively over the
437 west coast of Western Europe, the Western Europe, and the region from eastern
438 Mediterranean to the northwest of TP. This corresponds to a SAH center over Iranian
439 Plateau (Fig. 12a). With the eastward movement and intensification of the negative
440 PV anomalies along the SWJ north of the SAH from 26 to 30 July, the SAH center
441 shifts eastward toward TP and gets intensified, corresponding to simultaneously
442 eastward moving and strengthening of the northerly anomalies over the northeast of
443 the SAH center (Figs. 12a–c). The strengthened northerlies are followed by southward
444 high PV intrusion downstream of the SAH center, as manifested by the southward
445 deformation of the tropopause as well as the consequent positive PV anomalies north
446 of TP (Fig. 12c). On 1 August, accompanying the eastward movement of negative PV
447 anomalies over the north of TP, the SAH center has shifted to the western TP and
448 becomes stronger than before, leading to significantly northerly anomalies over the
449 north of TP (Fig. 12d). Under such favorable circulation conditions, TFs occur over
450 the eastern TP (Fig. 12d). From 1 to 3 August, with the further eastward movement of
451 negative PV anomaly center over the north of TP, the entire SAH body (marked by

452 12520 gpm) stretches longitudinally and extends eastward (Figs. 12d–e). Meanwhile,
453 the related northerly anomaly center moves from the north of TP to the northeast of
454 TP (Figs. 12d–e). Till 3 August, the TF–ETP occurs (Fig. 12e).

455 To further examine the existence of such remote linkage between the TF–ETP
456 and leading atmospheric perturbations over the NEA during this TF–ETP case, we
457 plot in Fig. 13 the geopotential height and its anomalies, and wave activity flux
458 anomalies at 200–hPa. As will be shown below, the remote linkage via a RWT can be
459 verified in this typical TF–ETP case. Specifically, it can be seen from Fig. 13a that, a
460 low anomaly center appears over the NEA since 26 July, and seems to act as the wave
461 source of a RWT propagating downstream to Caspian Sea region. In addition,
462 locations of the height anomaly centers along the RWT, as well as the wave activity
463 flux anomaly pattern, are very similar to those in the regressed results shown in Fig.
464 6b. On 30 July, the propagating RWT induces an anomalous high to the northwest of
465 Korean Peninsula, indicating a complete RWT stretching from the NEA to East Asia
466 (Fig. 13c). When the anomalous low over the NEA tends to gradually decrease after
467 30 July, the high anomaly center over Western Europe gradually increases and seems
468 to become the main wave source of the RWT (Figs. 13c–e). The RWT thus links the
469 low anomaly over the NEA to the TF–ETP occurrence.

470 **5. Summary**

471 By identifying TF–ETP events objectively, this study performs a comprehensive
472 composite and regressed analysis of TF–ETP occurred in the latest decades. We first
473 reveal the significant and typical impacts of TF–ETP occurrence on the circulation

474 and weather anomalies over East Asia, and then demonstrate that the TF–ETP
475 occurrence is closely related to an intensification of the SAH center over TP, which in
476 turn can be remotely connected to circulation anomalies over the NEA. Specifically,
477 although the frequency of TF–ETP occurrence is only about 3%, relatively lower than
478 the two hot TFs spots over the eastern Mediterranean region (10%) and the central
479 Asian region (8%) in summer, impacts of the TF–ETP occurrence, however, are
480 critical in China and East Asia. Frequent TF–ETP occurrence is associated with a
481 dipole rainfall anomaly pattern in China, with significantly negative rainfall
482 anomalies in the upper and middle reaches of the Yangtze and Yellow river valleys,
483 and positive rainfall anomalies in eastern China. In addition, Frequent TF–ETP
484 occurrence corresponds to a significantly stronger SAH center over TP, which in turn
485 induces anomalously strong upper–tropospheric northerlies and downward motion
486 over the northeast of TP, and thus enhanced southward and downward PV intrusion to
487 the east of TP.

488 Furthermore, the occurrence of TF–ETP, as well as the accompanied variation of
489 the SAH, is connected to leading circulation anomalies over the NEA several days
490 before via a RWT initiated from there. Around one week before the occurrence of
491 TF–ETP, a low anomaly center over the NEA becomes the strongest. This anomalous
492 low acts as the wave source of a RWT that propagates downstream along the SWJ. A
493 downstream high anomaly center is induced over the Caspian Sea region, which
494 gradually intensifies and moves eastward along the RWT. When this high anomaly
495 center arrives at the north edge of the SAH, it helps to intensify the SAH center and

496 forces it to shift eastward to the TP region. An anomalously stronger SAH center over
497 TP thus favors the TF–ETP occurrence because of the anomalously stronger
498 southward and downward PV intrusion caused by the stronger northerlies and descent
499 motion over the east of TP. Furthermore, the close relationship between TF–ETP
500 occurrence and SAH intensity, the rainfall anomaly pattern over East Asia during the
501 period of TF–ETP occurrence, as well as the remote connection to the circulation
502 anomalies over the NEA, are all verified in a typical TF–ETP case occurred in
503 summer 1990.

504 It should be noted that the TF–ETP–related RWT identified here may be related
505 to the recurrent teleconnection pattern which usually originates from the North
506 Atlantic region and goes along the SWJ across the Eurasian continent in boreal
507 summer (Ding and Wang 2005, 2007). In fact, some similar RWTs linking
508 atmospheric perturbations over North Atlantic to the circulation anomalies over
509 Eurasian continent were also identified in the intraseasonal and interannual timescales
510 in boreal summer (e.g., Chang et al. 2001; Hu et al. 2016; Yang and Li 2016; Zhu et
511 al. 2018). This study further demonstrates that the RWT is initiated from a low
512 anomaly center over the NEA, which may be induced by the anomalously stronger
513 dynamical forcing of transient eddy activities at the right side of the exit region of the
514 North American SWJ. The occurrence of TF–ETP is thus remotely related to the
515 circulation anomalies over the NEA.

516

517 **Acknowledgments** This work was jointly supported by the Strategic Priority

518 Research Program [grant number XDA17010105] of the Chinese Academy of
519 Sciences, the National Natural Science Foundation of China [grant numbers
520 91837311, 91437105].

521 **Funding** This work was funded by the Strategic Priority Research Program [grant
522 number XDA17010105] of the Chinese Academy of Sciences, the National Natural
523 Science Foundation of China [grant numbers 91837311, 91437105].

524 **Data availability** The ERA–interim reanalysis dataset can be accessed from the
525 website <http://apps.ecmwf.int/datasets/data/interim–full–daily/levtype=sfc/>. The CPC
526 precipitation dataset can be accessed from the website
527 <https://www.esrl.noaa.gov/psd/data/gridded/data.cpc.globalprecip.html>.

528 **Code availability** All the codes are programmed by NCAR Command Language
529 (NCL, version 6.6). The codes are available and maintained by Chuandong Zhu
530 (zcd@lasg.iap.ac.cn).

531 **Authors' contributions** Conceptualization: CDZ and RCR; methodology, CDZ and
532 RCR; software, CDZ; formal analysis, CDZ and RCR; investigation, CDZ and RCR;
533 resources, CDZ; writing-original draft preparation, CDZ; writing-review and editing,
534 RCR; visualization, CDZ; supervision, RCR. All authors read and approved the final
535 manuscript.

536 **Conflicts of interest/Competing interests** The authors declare no conflict of interest.

537
538

539 **References**

- 540 Akritidis, D., et al. (2016), On the role of tropopause folds in summertime
541 tropospheric ozone over the eastern Mediterranean and the Middle East, *Atmos.*
542 *Chem. Phys.*, 16, 14025–14039, doi:10.5194/acp-16-14025-2016.
- 543 Akritidis, D., A. Pozzer, and P. Zanis (2019), On the impact of future climate change
544 on tropopause folds and tropospheric ozone, *Atmos. Chem. Phys.*, 19,
545 14387–14401, doi:10.5194/acp-19-14387-2019.
- 546 Allen, J. T., A. B. Pezza, and M. T. Black (2010), Explosive cyclogenesis: A global
547 climatology comparing multiple reanalyses, *J. Clim.*, 23, 6468–6484,
548 doi:10.1175/2010JCLI3437.1.
- 549 Antonescu, B., G. Vaughan, and D.M. Schultz (2013), A Five-Year Radar-Based
550 Climatology of Tropopause Folds and Deep Convection over Wales, United
551 Kingdom, *Mon. Wea. Rev.*, 141, 1693–1707, doi:10.1175/MWR-D-12-00246.1.
- 552 Baray, J. L., V. Daniel, G. Ancellet, and B. Legras (2000), Planetary-scale tropopause
553 folds in the southern subtropics, *Geophys. Res. Lett.*, 27, 353–356,
554 doi:10.1067/mai.2000.108430.
- 555 Bjercknes, J., and E. Palmén (1937), Investigations of selected European cyclones by
556 means of serial ascents, *Geophys. Publ.*, 12, 1–62.
- 557 Blackmon, M. L. (1976), A climatological spectral study of the 500 mb geopotential
558 height of the Northern Hemisphere, *J. Atmos. Sci.*, 33, 1607–1623, doi:
559 10.1175/1520-0469(1976)0332.0.CO;2.
- 560 Bourqui, M. S. and P. Y. Trepanier (2010), Descent of deep stratospheric intrusions
561 during the IONS August 2006 campaign, *J. Geophys. Res.*, 115,
562 doi:10.1029/2009JD013183.
- 563 Browning, K. A., and B. W. Golding (1995), Mesoscale aspects of a dry intrusion
564 within a vigorous cyclone, *Quart. J. Roy. Meteor. Soc.*, 121, 463–493,
565 doi:10.1002/qj.49712152302.
- 566 Browning, K. A., and R. Reynolds (1994), Diagnostic study of a narrow cold-frontal
567 rainband and severe winds associated with a stratospheric intrusion, *Quart. J.*
568 *Roy. Meteor. Soc.*, 120, 235–257, doi:10.1002/qj.49712051602.
- 569 Chen, M., et al. (2008), Assessing objective techniques for gauge-based analyses of
570 global daily precipitation, *J. Geophys. Res.*, 113, D04110,
571 doi:10.1029/2007JD009132.
- 572 Chen, P. (1995), Isentropic cross-tropopause mass exchange in the extratropics, *J.*
573 *Geophys. Res.*, 100, 16661–16673, doi:10.1029/95JD01264.
- 574 Cooper, O. R., et al. (2005), Direct transport of midlatitude stratospheric ozone into
575 the lower troposphere and marine boundary layer of the tropical Pacific Ocean, *J.*

-
- 576 *Geophys. Res.*, 110, 23310(1–15), doi:10.1029/2005JD005783.
- 577 Cui, Q., C. M. Wang, and Y. Zhang (2016), Analysis of impact of dry intrusion in a
578 strong squall line process in eastern China, *Desert and Oasis–Meteorology* (in
579 Chinese), 10, 18–24, doi:10.3969/j.issn.1002–0799.2016.02.003.
- 580 Dafka, S., D. Akritidis, P. Zanis, et al. (2020), On the link between the Etesian winds,
581 tropopause folds and tropospheric ozone over the Eastern Mediterranean during
582 summer. *Atmos. Environ.*, 248, 1–12, doi:10.1016/j.atmosres.2020.105161.
- 583 Dee, D. P., et al. (2011), The ERA–Interim reanalysis: Configuration and performance
584 of the data assimilation system, *Quart. J. Roy. Meteor. Soc.*, 137, 553–597,
585 doi:10.1002/qj.828.
- 586 Ding, Q. H., and B. Wang (2007), Intraseasonal teleconnection between the summer
587 Eurasian wave train and the Indian monsoon, *J. Clim.*, 20, 3751–3767,
588 doi:10.1175/JCLI4221.1.
- 589 Ding, Q. H., and B. Wang (2005), Circumglobal teleconnection in the Northern
590 hemisphere summer, *J. Clim.*, 18, 3483–3505, doi:10.1175/JCLI3473.1.
- 591 Ebel, A., et al. (1991), Simulation of ozone intrusion caused by a tropopause fold and
592 cut-off low, *Atmos. Environ.*, 25, 2131–2144,
593 doi:10.1016/0960–1686(91)90089–P.
- 594 Elbern, H., J. Hendricks, and A. Ebel (1998), A climatology of tropopause folds by
595 global analyses, *Theor. Appl. Climatol.*, 59, 181–200,
596 doi:10.1007/s007040050023.
- 597 Ertel, H. (1942), A new hydrodynamical vorticity equation, *Meteorologische*
598 *Zeitschrift*, 59, 33–49.
- 599 Fadnavis, S. and R. Chattopadhyay (2017), Linkages of Subtropical Stratospheric
600 Intraseasonal Intrusions with Indian Summer Monsoon Deficit Rainfall, *J. Clim.*,
601 30, 5083–5095, doi:10.1175/JCLI–D–16–0463.1.
- 602 Forster, C., and V. Wirth (2000), Radiative decay of idealized stratospheric filaments
603 in the troposphere, *J. Geophys. Res.*, 105, 10169–10184,
604 doi:10.1029/2000JD900052.
- 605 Goering, M. A., W. A. Gallus, M. A. Olsen, and J. L. Stanford (2001), Role of
606 stratospheric air in a severe weather event: Analysis of potential vorticity and
607 total ozone, *J. Geophys. Res.*, 106, 11813–11823, doi:10.1029/2000JD900651.
- 608 Gouget, H., G. Vaughan, A. Marenco, and H. G. J. Smit (2000), Decay of a cut-off
609 low and contribution to stratosphere–troposphere exchange, *Quart. J. Roy.*
610 *Meteor. Soc.*, 126, 1117–1141, doi:10.1002/qj.49712656414.
- 611 Griffiths, M., A. J. Thorpe, and K. A. Browning (2000), Convective destabilization by
612 a tropopause fold diagnosed using potential–vorticity inversion, *Quart. J. Roy.*
613 *Meteor. Soc.*, 126, 125–144, doi:10.1002/qj.49712656207.

-
- 614 Hofmann, C., et al. (2016), Stratosphere–troposphere exchange in the vicinity of a
615 tropopause fold, *Atmos. Chem. Phys.*, 1–26, doi:10.5194/acp–2015–949.
- 616 Holopainen, E. O., L. Rontu, and N. C. Lau (1982), The effect of large-scale transient
617 eddies on the time-mean flow in the atmosphere, *J. Atmos. Sci.*, 39, 1972–1984,
618 doi:10.1175/1520-0469(1982)0392.0.CO;2.
- 619 Holton, J. R., P. H. Haynes, M. E. McIntyre, A. R. Douglass, R. B. Rood, and L.
620 Pfister (1995), Stratosphere–troposphere exchange, *Rev. Geophys.*, 33, 403–440,
621 doi:10.1029/95RG02097.
- 622 Hoskins, B. J., M. Pedder, and D. W. Jones (2003), The omega equation and potential
623 vorticity, *Quart. J. Roy. Meteor. Soc.*, 129, 3277–3303, doi:10.1256/qj.02.135.
- 624 Hoskins, B. J. (1997), A potential vorticity view of synoptic development, *Meteor.*
625 *Appl.*, d, 325–334, doi:10.1017/S1350482797000716.
- 626 Hoskins, B. J., and T. Ambrizzi (1993), Rossby Wave Propagation on a Realistic
627 Longitudinally Varying Flow, *J. Atmos. Sci.*, 50,
628 1661–1671, doi:10.1175/1520–0469(1993)050<1661:RWPOAR>2.0.CO;2.
- 629 Hoskins, B. J., P. J. Valdes (1990), On the existence of storm-tracks, *J. Atmos. Sci.*, 47,
630 1854–1864, doi:10.1175/1520-0469(1990)047<1854:OTEOST>2.0.CO;2.
- 631 Hoskins, B. J., M. E. McIntyre, and A. W. Robertson (1985), On the use and
632 significance of isentropic potential vorticity maps, *Quart. J. Roy. Meteor. Soc.*,
633 111, 877–946, doi:10.1002/qj.49711147002.
- 634 Hoskins, B. J., and D. J. Karoly (1981), The steady linear response of a spherical
635 atmosphere to thermal and orographic forcing, *J. Atmos. Sci.*, 38, 1179–1196,
636 doi:10.1175/1520–0469(1981)038<1179:TSLROA>2.0.CO;2.
- 637 Hsu, C. J., R. A. Plumb (2000), Nonaxisymmetric thermally driven circulations and
638 upper–tropospheric monsoon dynamics, *J. Atmos. Sci.*, 57, 1255–1276,
639 doi:10.1175/1520–0469(2000)057<1255:NTDCAU>2.0.CO;2.
- 640 Hu, W. T., et al. (2016) The intraseasonal oscillation of eastern Tibetan Plateau
641 precipitation in response to the summer Eurasian wave train, *J. Clim.*, 29,
642 7215–7230, doi:10.1175/JCLI-D-15-0620.1.
- 643 Keyser, D., and M. A. Shapiro (1986), A review of the structure and dynamics of
644 upper–level frontal zones, *Mon. Wea. Rev.*, 114, 452–499,
645 doi:10.1175/1520–0493(1986)114<0452:AROTSA>2.0.CO;2.
- 646 Kim, J., et al. (2013), A Case Study of Mesoscale Snowfall Development Associated
647 with Tropopause Folding, *Atmos.*, 23, 331–346,
648 doi:10.14191/Atmos.2013.23.3.331.
- 649 Krishnamurti, T. N., and H. N. Bhalme (1976), Oscillations of a monsoon system. Part
650 I. observational aspects. *J. Atmos. Sci.*, 33, 1937–1954,
651 doi:10.1175/1520-0469(1976)033%3C1937:OOAMS P%3E2.0.CO;2.

-
- 652 Krishnamurti, T. N., and P. Ardanuy (1980), The 10 to 20-day westward propagating
653 mode and “Breaks in the Monsoons, *Tellus*, 1, 15–26,
654 doi:10.3402/tellusa.v32i1.10476.
- 655 Lamarque, J. F., and P. G. Hess (1994), Cross-tropopause mass exchange and
656 potential vorticity budget in a simulated tropopause folding, *J. Atmos. Sci.*, 51,
657 2246–2269, doi:10.1175/1520-0469.
- 658 Lau, N. C. (1978). On the three-dimensional structure of the observed transient eddy
659 statistics of the northern Hemisphere wintertime circulation, *J. Atmos. Sci.*, 35,
660 1854–1864, doi:10.1175/1520-0469(1978)035<1900:OTTDSO>2.0.CO;2.
- 661 Lau, N. C., and E. O. Holopainen (1984), Transient eddy forcing of the time-mean
662 flow as identified by geopotential tendencies, *J. Atmos. Sci.*, 41, 313–328,
663 doi:10.1175/1520-0469(1984)041,0313:TEFOTT.2.0.CO;2.
- 664 Lau, N. C., and M. J. Nath (1991), Variability of the baroclinic and barotropic
665 transient eddy forcing associated with monthly changes in the midlatitude storm
666 tracks, *J. Atmos. Sci.*, 48, 258–2613,
667 doi:10.1175/1520-0469(1991)048,2589:VOTBAB.2.0.CO;2.
- 668 Lelieveld, J., and F. J. Dentener (2000), What controls tropospheric ozone? *J.*
669 *Geophys. Res.*, 105, 3531–3551, doi:10.1029/1999JD901011.
- 670 Liu, H. R., and C. Y. Li (2010), Impacts of the Dry Intrusion on Jinan Torrential Rain
671 Occurring on 18 July 2007, *Chin. J. Atmos. Sci.* (in Chinese), 34, 374–386,
672 doi:10.3878/j.issn.1006-9895.2010.02.11.
- 673 Liu, Y. M., et al. (2001), Condensation heating of the Asian summer monsoon and the
674 subtropical anticyclone in the Eastern Hemisphere, *Clim. Dyn.*, 17, 327–338,
675 doi:10.1007/s003820000117.
- 676 Liu, Y. M., B. J. Hoskins, and M. Blackburn (2007), Impact of Tibetan orography and
677 heating on the summer flow over Asia, *J. Meteor. Soc. Jpn.*, 85, 1–19,
678 doi:10.2151/jmsj.85B.1.
- 679 Morcrette, C., et al. (2007), Combination of Mesoscale and Synoptic Mechanisms for
680 Triggering an Isolated Thunderstorm: Observational Case Study of CSIP IOP 1,
681 *Mon. Wea. Rev.*, 135, 3728–3749, doi:10.1175/2007MWR2067.1.
- 682 Mullen, S. L. (1987), Transient eddy forcing of blocking flows, *J. Atmos. Sci.*, 44,
683 3–22, doi:10.1175/1520-0469(1987)044,0003:TEFOBF.2.0.CO;2.
- 684 Ortega, S., et al. (2017), Quasi-biweekly oscillations of the South Asian monsoon and
685 its co-evolution in the upper and lower troposphere, *Clim. Dyn.*, 49, 1–16,
686 doi:10.1007/s00382-016-3503-y.
- 687 Plumb, R. A. (1985), On the three-dimensional propagation of stationary waves, *J.*
688 *Atmos. Sci.*, 42, 217–229,
689 doi:10.1175/1520-0469(1985)042<0217:OTTDPO>2.0.CO;2.

-
- 690 Popovic, J. M., R. A. Plumb (2001), Eddy Shedding from the Upper–Tropospheric
691 Asian Monsoon Anticyclone, *J. Atmos. Sci.*, 58, 93–105,
692 doi:10.1175/1520–0469(2001)058<0093:ESFTUT>2.0.CO;2.
- 693 Reed, R. J. (1955), A study of a characteristic type of upper–level frontogenesis, *J.*
694 *Atmos. Sci.*, 12, 226–237,
695 doi:10.1175/1520–0469(1955)012<0226:ASOACT>2.0.CO;2.
- 696 Ren, R. C., et al. (2014), Progresses in stratosphere–troposphere interactions:
697 application of isentropic potential vorticity dynamics and effect of the Tibetan
698 Plateau, *J. Meteor. Res.*, 28 714–731, doi:10.1007/s13351–014–4026–2.
- 699 Ren, R. C., C. D. Zhu, and M. Cai (2019), Linking quasi–biweekly variability of the
700 South Asian high to atmospheric heating over Tibetan Plateau in summer, *Clim.*
701 *Dyn.*, 53, 3419–3429, doi:10.1007/s00382–019–04713–4.
- 702 Ren, X. J., D. Yang, X. Q. Yang (2015), Characteristics and mechanism of
703 subseasonal eastward extension of South Asian high, *J. Clim.*, 28,
704 6799–6822, doi:10.1175/JCLI–D–14–00682.1.
- 705 Russell, A., G. Vaughan, and E. G. Norton (2012), Large–scale potential vorticity
706 anomalies and deep convection, *Quart. J. Roy. Meteor. Soc.*, 138, 1627–1639,
707 doi:10.1002/qj.1875.
- 708 Sanders, F., and J. R. Gyakum (1980), Synoptic–dynamic climatology of the “bomb”,
709 *Mon. Wea. Rev.*, 108, 1589–1606, doi:10.1175/1520–0493(1980)1082.0.CO;2.
- 710 Sawyer, J. S. (1956), The vertical circulation at meteorological fronts and its relation
711 to frontogenesis, *Proc. R. Soc. Lond. A*, 234, 346–362,
712 doi:10.1098/rspa.1956.0039.
- 713 Schmidt, T., et al. (2006), A climatology of multiple tropopause derived from GPS
714 radio occultations with CHAMP and SAC–C, *Geophys. Res. Lett.*, 33, L04808,
715 doi:10.1029/2005GL024600.
- 716 Shapiro, M. A. (1981), Frontogenesis and geostrophically forced secondary
717 circulations in the vicinity of jet stream–frontal zone systems, *J. Atmos. Sci.*, 38,
718 954–973, doi:10.1175/1520–0469(1981)038<0954:FAGFSC>2.0.CO;2.
- 719 Shapiro, M. A. (1980), Turbulent mixing within tropopause folds as a mechanism for
720 the exchange of chemical constituents between the stratosphere and
721 troposphere, *J. Atmos. Sci.*, 37, 994–1004,
722 doi:10.1175/1520–0469(1980)037<0994:TMWTFA>2.0.CO;2.
- 723 Shou, Y. X., et al. (2014), A New Method for Tropopause Folding Detection and Its
724 Application in Middle–Latitude Disastrous Weather Forecasting, *Chin. J. Atmos.*
725 *Sci.* (in Chinese), 38, 1109–1123, doi:10.3878/j.issn.1006–9895.1403.13258.
- 726 Škerlak, B., et al. (2015), Tropopause folds in ERA–Interim: Global climatology and
727 relation to extreme weather events, *J. Geophys. Res.*, 120, 4860–4877,

728 doi:10.1002/2014JD022787.

729 Škerlak, B., M. Sprenger, and H. Wernli (2014), A global climatology of
730 stratosphere–troposphere exchange using the ERA–Interim data set from 1979 to
731 2011, *Atmos. Chem. Phys.*, 14, 913–937, doi:10.5194/acp–14–913–2014.

732 Sorensen, J. H., and N. W. Nielsen (2001), Intrusion of stratospheric ozone to the free
733 troposphere through tropopause folds – A case study, *Phys. Chem.*, 26, 801–806,
734 doi:10.1016/S1464–1909(01)00088–0.

735 Sprenger, M., M. C. Maspoli, and H. Wernli (2003), Tropopause folds and
736 cross–tropopause exchange: a global investigation based upon ecmwf analyses
737 for the time period march 2000 to february 2001, *J. Geophys. Res.*, 108, 8518,
738 doi:10.1029/2002JD002587, 2003.

739 Stohl, A., et al. (2003), Stratosphere–troposphere exchange: a review, and what we
740 have learned from staccato, *J. Geophys. Res.*, 108, 469–474,
741 doi:10.1029/2002JD002490.

742 Terao, T. (1999), The Zonal Wavelength of the Quasi–Stationary Rossby Waves
743 Trapped in the Westerly Jet, *J. Meteor. Soc. Jpn.*, 77, 687–699,
744 doi:10.2151/jmsj1965.77.3_687.

745 Thorpe, A. J. (1997), Attribution and its application to mesoscale structure associated
746 with tropopause folds, *Quart. J. Roy. Meteor. Soc.*, 123, 2377–2399,
747 doi:10.1002/qj.49712354411.

748 Traub, M., and J. Lelieveld (2003), Cross–tropopause transport over the eastern
749 Mediterranean, *J. Geophys. Res.*, 108, 4712, doi:10.1029/2003JD003754.

750 Tyrlis, E., et al. (2014), On the linkage between the Asian summer monsoon and
751 tropopause fold activity over the eastern Mediterranean and the Middle East, *J.*
752 *Geophys. Res.*, 119, 3202–3221, doi:10.1002/2013JD021113.

753 Tyrlis, E., J. Lelieveld, and B. Steil (2013), The summer circulation over the eastern
754 Mediterranean and the Middle East: influence of the South Asian monsoon, *Clim.*
755 *Dyn.*, 40, 1103–1123, doi:10.1007/s00382–012–1528–4.

756 Uccellini, L. W. (1990), Processes contributing to the rapid development of
757 extratropical cyclones, in *Extratropical Cyclones, The Erik Palmén Memorial*
758 *Volume*, edited by C. Newton and E. Holopainen, pp. 81–105, *Am. Meteorol.*
759 *Soc.*, Boston, Mass.

760 Vaughan, G., et al. (2017), Invigoration and Capping of a Convective Rainband ahead
761 of a Potential Vorticity Anomaly, *Mon. Wea. Rev.*, 145, 2093–2117, doi :
762 10.1175/MWR–D–16–0397.1.

763 Vogel, B., et al. (2014), Fast transport from Southeast Asia boundary layer sources to
764 northern Europe: rapid uplift in typhoons and eastward eddy shedding of the
765 Asian monsoon anticyclone, *Atmos. Chem. Phys.*, 14, 12745–12762,

-
- 766 doi:10.5194/acpd-14-18461-2014.
- 767 Wernli, H., S. Dirren, M. A. Liniger, and M. Zillig (2002), Dynamical aspects of the
768 life cycle of the winter storm “Lothar” (24–26 December 1999), *Quart. J. Roy.*
769 *Meteor. Soc.*, 128, 405–429, doi:10.1256/003590002321042036.
- 770 Wu, G. X., and Y. M. Liu (2000), Thermal adaptation, dispersion, and subtropical
771 anticyclone Part I: Thermal adaptation and overshooting, *Chi. J. Atmos. Sci.* (in
772 Chinese), 24, 433–446, doi:10.3878/j.issn.1006-9895.2000.04.01.
- 773 Wu, Y. T., et al. (2018), On the linkage between the Asian summer monsoon and
774 tropopause folds, *J. Geophys. Res.*, 123, 2037–2049.
775 doi:10.1002/2017JD027870.
- 776 Xia, X., et al. (2016), An analysis on the spatio-temporal variations and dynamic
777 effects of the tropopause and the related stratosphere-troposphere coupling
778 surrounding the Tibetan Plateau area, *Acta Meteor. Sin.*, 74, 525–541,
779 doi:10.11676/qxxb2016.036.
- 780 Xu, P. Q., L. Wang, and W. Chen (2018), The British-Baikal Corridor: A
781 teleconnection pattern along the summertime polar front jet over Eurasia, *J.*
782 *Clim.*, 32, 877–896, doi:10.1175/JCLI-D-18-0343.1.
- 783 Yanai, M., E. Steven, and J. H. Chu (1973), Determination of bulk properties of
784 tropical cloud clusters from large-scale heat and moisture budgets, *J. Atmos. Sci.*,
785 30, 611–627, doi:10.1175/1520-0469(1973)030<0611:DOBPOT>2.0.CO;2.
- 786 Yang, S. Y., T. Li (2016), Zonal shift of the South Asian High on the subseasonal
787 time-scale and its relation to the summer rainfall anomaly in China, *Quart. J.*
788 *Roy. Meteor. Soc.*, 142, 2324–2335, doi:10.1002/qj.2826.
- 789 Zhao, D. J., and X. P. Yao (2017), Characteristics of the Dry Intrusion Index in an
790 extreme torrential rain event occurred on 21 July 2012 in Beijing, *Torrential*
791 *Rain and Disasters* (in Chinese), 36, 527–534,
792 doi:10.3969/j.issn.1004-9045.2017.06.005.
- 793 Zhu, C. D., R. C. Ren, and G. X. Wu (2018), Varying Rossby wave trains from the
794 developing to decaying period of the upper atmospheric heat Source over the
795 Tibetan Plateau in boreal summer, *Adv. Atmos. Sci.*, 35, 1114–1128,
796 doi:10.1007/s00376-017-7231-y.

797

798

799

800

801

802

803
804
805
806
807
808
809
810
811
812
813
814
815
816
817
818
819
820

821 **Figure Captions**

822 **Fig. 1** (a) Summertime (July-August) climatology of tropopause folding frequency
823 (shaded; units: %), geopotential height (brown contours; units: gpm; interval: 10) and
824 westerly jet speed (black contours; units: m s^{-1} ; above 20 m s^{-1}) at 200-hPa. The TP's
825 topographic boundary of 1500 m is marked with thin black solid line, and the Yellow
826 and Yangtze River from north to south is marked with blue lines. (b) Daily variation
827 of the TFI for the 40 summers (July–August). The abscissa represents the time in year
828 and the vertical red dashed lines indicate 1 July of every year. (c) Power spectrum
829 (solid line) of the normalized daily TFI derived from data in the 40 summers. The
830 short and long dashes mark the 99% confidence level and the red noise spectrum
831 respectively.

832

833 **Fig. 2** Vertical cross-sections of (a, b) composite potential temperature (red dashed
834 contours; units: K; interval: 10), PV (blue contours; units: PVU; only values of 1 and
835 2 PVU are plotted) and its anomalies (shaded; units: PVU); and (c, d) composite
836 horizontal divergence anomalies (black contours; units: 10^{-6} s^{-1} ; interval: 1; value of

837 zero is neglected), vertical motion ω (shaded; units: 10^{-2} Pa s^{-1}) anomalies and PV
838 (blue contours; units: PVU; only values of 1 and 2 PVU are plotted) for high TFI days.
839 The left and right column are for the vertical-longitudinal cross-section along 39° N
840 and the vertical-latitude cross-section along 111° E respectively. Black contours in
841 (a, b) denote the corresponding summer climatology of 1 and 2 PVU surfaces.
842 Stippled in (a, b) and (c, d) indicate the 90% confidence level of the composite
843 potential vorticity anomalies and vertical motion anomalies respectively. Areas shaded
844 in black show the topography.

845

846 **Fig. 3** Composites of (a) PV anomalies (shaded; units: PVU; only those above 90%
847 confidence level are plotted) and horizontal wind anomalies (vector; units: $m\ s^{-1}$) at
848 300–hPa; (b) horizontal divergence anomalies (shaded; units: $10^{-6}\ s^{-1}$) and horizontal
849 wind anomalies (vector; units: $m\ s^{-1}$) at 700–hPa; (c) rainfall anomalies (shaded; units:
850 mm) for high TFI days. Stippling areas in (b) and (c) indicate the 90% confidence
851 level of the composite horizontal divergence anomalies and rainfall anomalies,
852 respectively. Black arrows in (b) indicate the 90% confidence level of the composite
853 horizontal wind anomalies.

854

855 **Fig. 4** Composite TF frequency (shaded; units: %), geopotential height (brown
856 contours; units: gpm; interval: 10; 12520 gpm above) and westerly wind speed (black
857 contours; units: $m\ s^{-1}$; 20 $m\ s^{-1}$ above) at 200–hPa for high TFI days. The thin black
858 solid contour marks the TP's topographic boundary of 1500 m. The blue curves
859 delineate the Yellow and Yangtze River from north to south.

860

861 **Fig. 5** Composite (a) meridional wind (contours; units: $m\ s^{-1}$; interval: 1; Value of zero
862 is neglected) and vertical motion ω (shaded; units: 10^{-2} Pa s^{-1}) anomalies at 200–hPa;
863 (b) geopotential height (brown contours; units: gpm; interval: 10; 12520 gpm above)
864 and its anomalies (shaded; units: gpm), westerly wind speed (black contours; units: $m\ s^{-1}$;
865 20 $m\ s^{-1}$ above), and wave activity flux (vector; units: $10^{-1}\ m^2\ s^{-2}$; amplitudes
866 larger than 0.05 are shown) anomalies at 200–hPa for high TFI days. The Stippling
867 and hatched areas in (a) indicate the 90% confidence level of composite meridional
868 wind and vertical motion anomalies, respectively. The Stippling areas in (b) indicate
869 the 90% confidence level of the composite geopotential height anomalies.

870

871 **Fig. 6** Lead/lag regressions against the PVI of geopotential height (black contours;
872 units: gpm; interval 4; value of zero is ignored), vertical motion ω (shaded; units: 10^{-2}
873 Pa s^{-1} ; only the statistical significance at 90% confidence level is plotted), and wave
874 activity flux anomalies (vector; units: $10^{-1}\ m^2\ s^{-2}$; amplitudes larger than 0.5 are shown)
875 at 200–hPa, when the PVI leads for (a) –7 days, (b) –6 days, (c) –5 days, (d) –4
876 days, (e) –3 days, (f) –2 days, (g) –1 day, and (h) 0 day. The red contours denote

877 the westerly jet that is stronger than 20 m s^{-1} at 200-hPa. The stippling areas indicate
878 the 90% confidence level of the regressed geopotential height anomalies.

879

880 **Fig. 7** As in Fig. 6 but for the PV (shaded; units: PVU; statistical significance at 90%
881 confidence level), meridional PV advection (black contours; units: PVU s^{-1} ; interval:
882 0.4), and meridional wind anomalies (vector; units: m s^{-1} ; only the vectors that are
883 statistically significant at 95% confidence level are plotted) at 200-hPa. The stippling
884 areas indicate the 90% confidence level of the regressed meridional PV advection
885 anomalies.

886

887 **Fig. 8** (a) Temporal evolution of the lead regressions against the PVI from day -10 to
888 day 0, of transient eddy kinetic energy (shaded; units: $\text{m}^2 \text{ s}^{-2}$) and vorticity advection
889 (contours; units: 10^{-6} m s^{-2} ; interval 2) anomalies at 300-hPa along the northern North
890 Atlantic (32° – 58°N); (b) Geographical distribution of the regressed transient eddy
891 kinetic energy (shaded; units: $\text{m}^2 \text{ s}^{-2}$) and vorticity advection (contours; units: 10^{-6} m
892 s^{-2} ; interval 2; value of zero is ignored) anomalies at 300-hPa at day -7. The red
893 contours denote the westerly jet (units: m s^{-1} ; interval: 4; values above 20 are plotted)
894 at 300-hPa. Stipplings and slashes in (a) and (b) indicate the 90% confidence level of
895 the regressions respectively for the transient eddy kinetic energy and vorticity
896 advection anomalies.

897

898 **Fig. 9** Vertical cross sections of (a) the regressed horizontal divergence (shaded; units:
899 10^{-6} s^{-1}), relative vorticity (contours; units: 10^{-6} s^{-1}), and vertical motion ω anomalies
900 (vectors; units: $10^{-3} \text{ Pa s}^{-1}$); and (b) the regressed air temperature (shaded; units: $^{\circ}\text{C}$),
901 and geopotential height (contours; units: gpm) anomalies against the PVI along 48°N
902 over the northern North Atlantic at day -7. Stipplings indicate the 90% confidence
903 level of the regression for (a) the horizontal divergence anomalies and (b) the air
904 temperature anomalies, respectively. The ordinate in (a, b) is the pressure level (units:
905 hPa).

906

907 **Fig. 10** Distribution of (a) the tropopause (2 PVU contour, bold brown), PV anomalies
908 (shaded; units: PVU) on 350K isentropic surface, and (b) horizontal wind anomalies
909 (vector; units: m s^{-1}) at 700-hPa and precipitation anomalies (shaded; units: mm d^{-1})
910 on 3 August, 1990.

911

912 **Fig. 11** Vertical cross sections of (a, b) potential temperature (red dashed contours;
913 units: K; interval: 10), PV (blue contours; units: PVU; only values of 1 and 2 PVU are
914 plotted) and its anomalies (shaded; units: PVU) on 3 August, 1990; and (c, d)
915 horizontal divergence anomalies (black contours; units: 10^{-6} s^{-1} ; interval: 4; value of
916 zero is neglected), vertical motion ω (shaded; units: $10^{-2} \text{ Pa s}^{-1}$) anomalies and PV
917 (blue contours; units: PVU; only values of 1 and 2 PVU are plotted) on 3 August,
918 1990. The left and right column are for the vertical-longitudinal cross-section along

919 37.5°N and the vertical-latitudinal cross-section along 109°E respectively. Black
920 contours in (a,b) are the corresponding summer climatology of 1 and 2 PVU. Areas
921 shaded in black show the topography.

922

923 **Fig. 12** Distribution of PV (shaded; units: PVU), the tropopause (2 PVU contour, bold
924 brown) and the meridional wind anomalies (blue contours; units: m s^{-1} ; interval: 6;
925 value of zero is neglected) at 350K isentropic surface, black dots mark the locations
926 where tropopause folding occurred; And geopotential height at 200 hPa (red contours;
927 units: gpm; interval: 10; above 12520 gpm) on (a) 26 July, (b) 28 July, (c) 30 July, (d)
928 1 August and (e) 3 August, 1990, respectively.

929

930 **Fig. 13** Spatial distribution of geopotential height (brown contours; units: gpm) and
931 its anomalies (black contours; units: gpm; interval: 10; value of zero is neglected), and
932 wave activity flux (vector; units: $10^2 \text{ m}^2 \text{ s}^{-2}$; amplitudes larger than 8 are shown) on (a)
933 26 July, (b) 28 July, (c) 30 July, (d) 1 August and (e) 3 August, 1990, respectively.

934

935

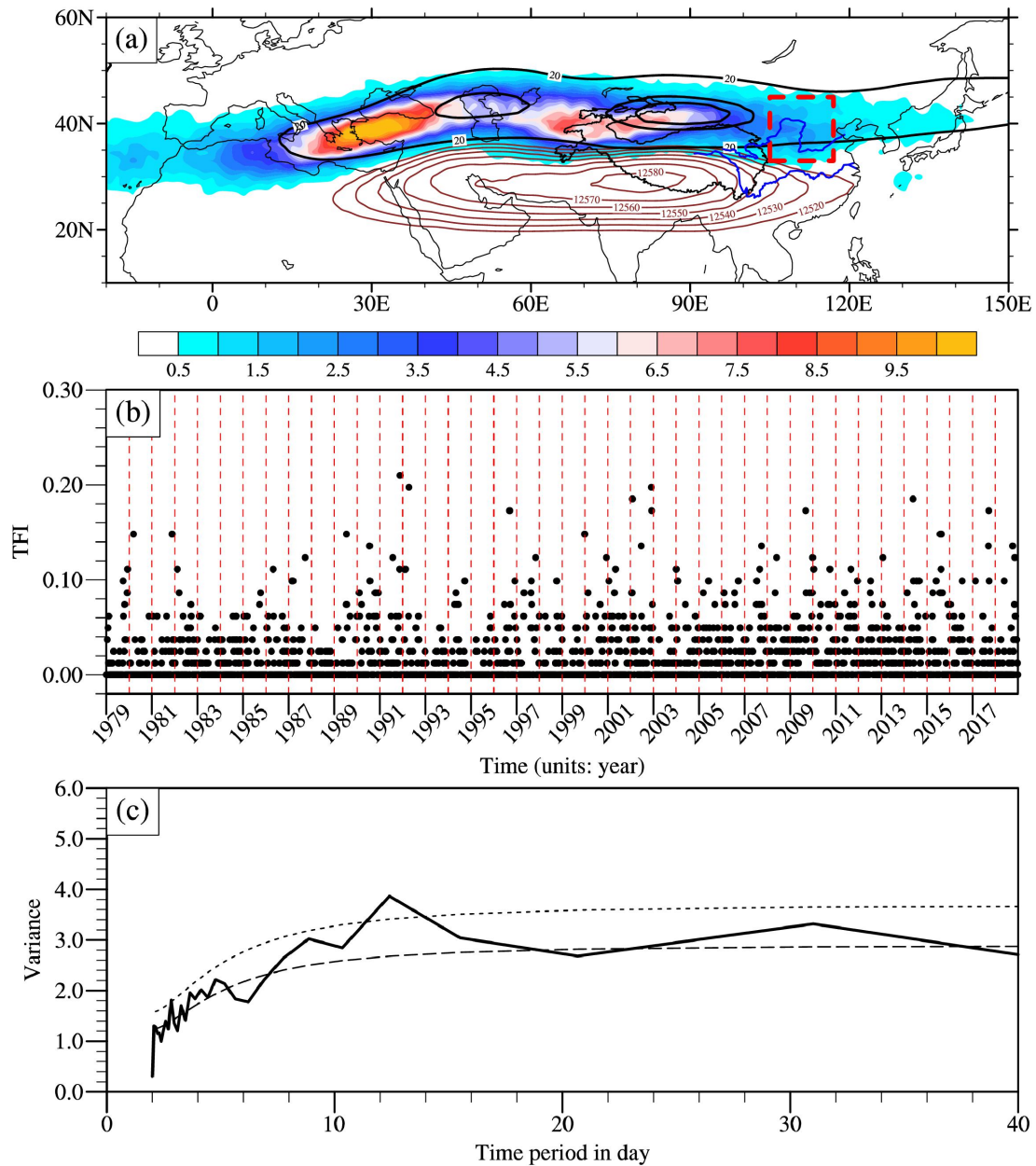
936

937

938

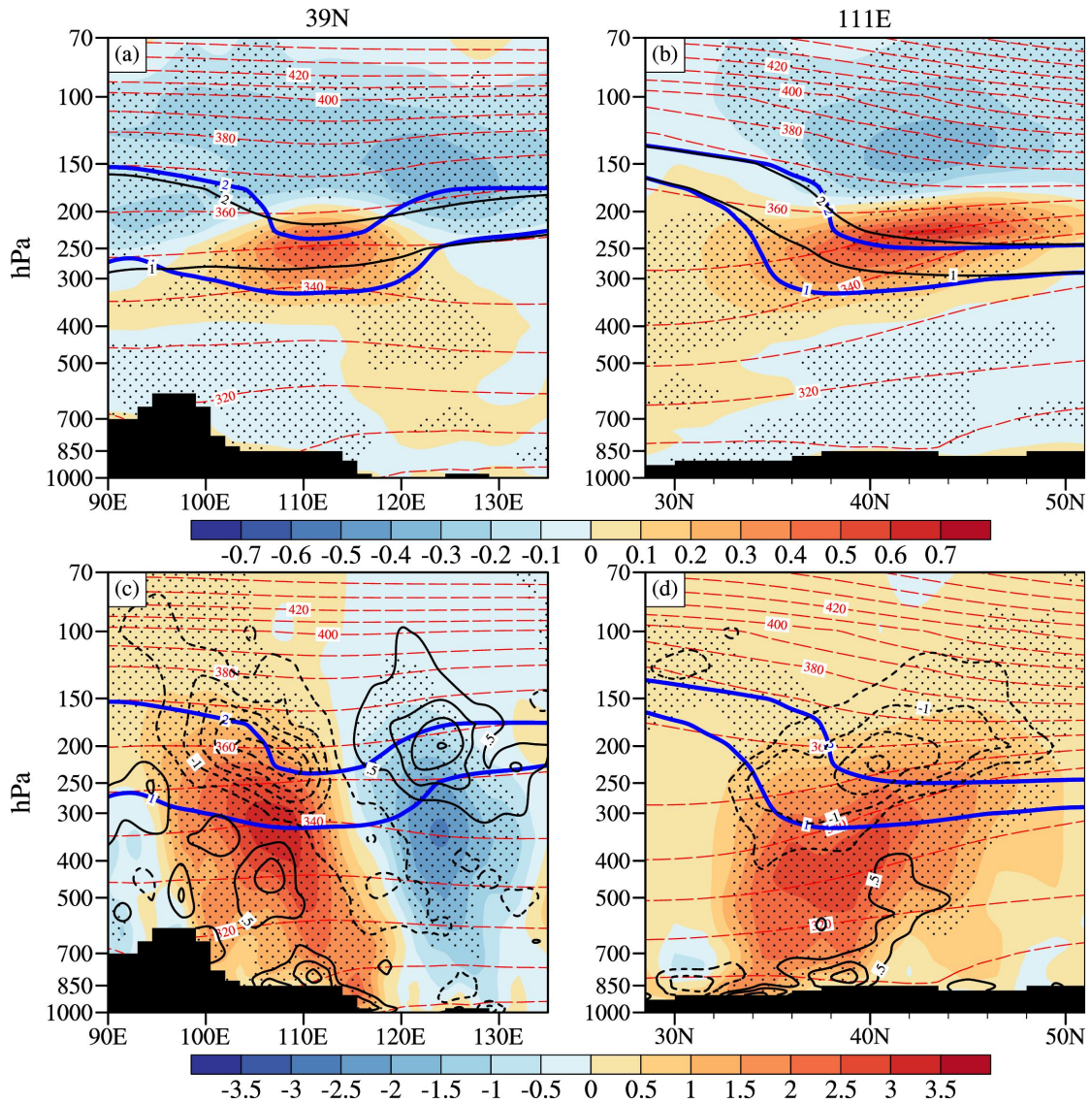
939

940 **Figures**



941

942 **Fig. 1** (a) Summertime (July-August) climatology of tropopause folding frequency
 943 (shaded; units: %), geopotential height (brown contours; units: gpm; interval: 10) and
 944 westerly jet speed (black contours; units: m s⁻¹; above 20 m s⁻¹) at 200-hPa. The TP's
 945 topographic boundary of 1500 m is marked with thin black solid line, and the Yellow
 946 and Yangtze River from north to south is marked with blue lines. (b) Daily variation
 947 of the TFI for the 40 summers (July–August). The abscissa represents the time in year
 948 and the vertical red dashed lines indicate 1 July of every year. (c) Power spectrum
 949 (solid line) of the normalized daily TFI derived from data in the 40 summers. The
 950 short and long dashes mark the 99% confidence level and the red noise spectrum
 951 respectively.



952

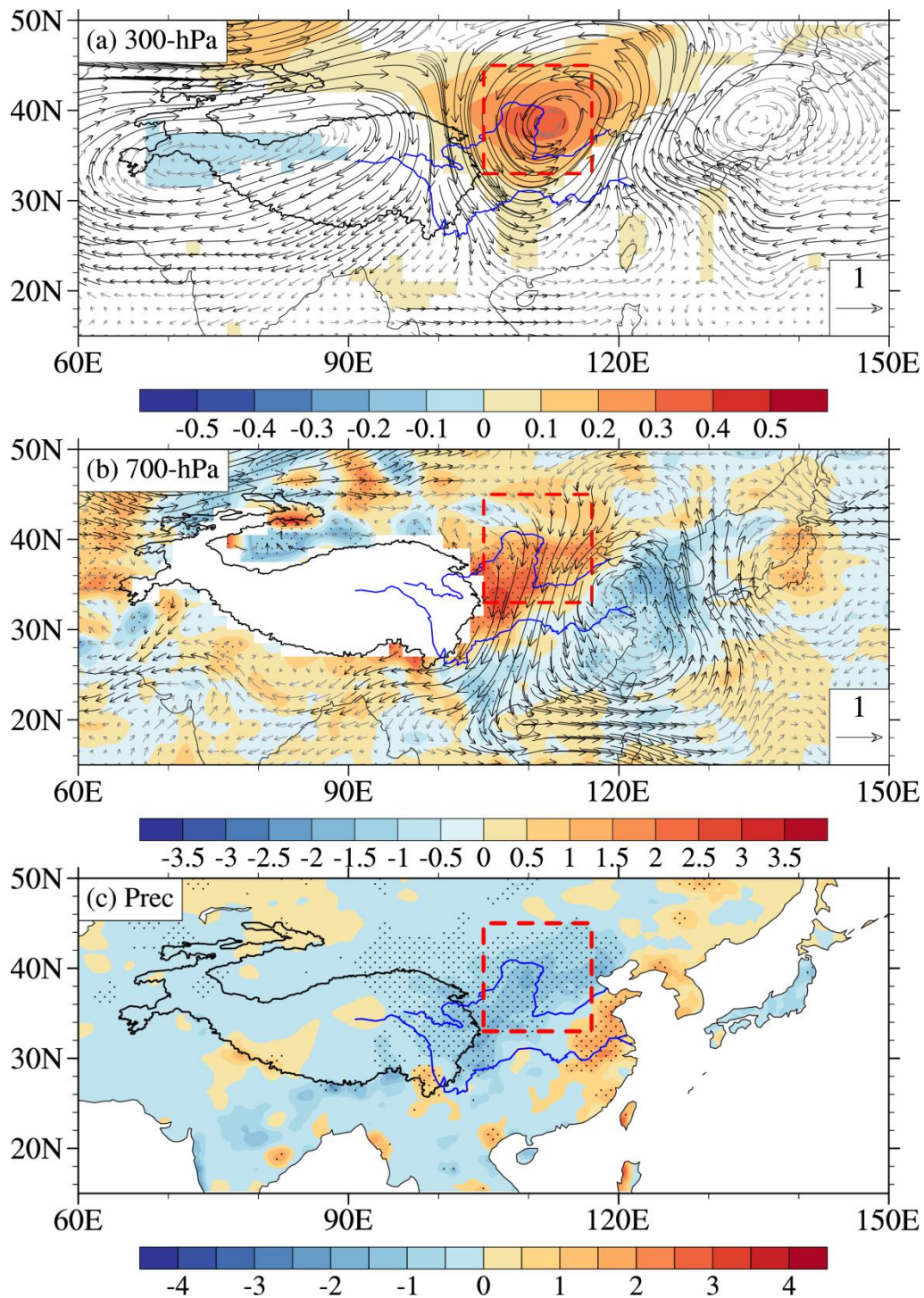
953 **Fig. 2** Vertical cross-sections of (a, b) composite potential temperature (red dashed
 954 contours; units: K; interval: 10), PV (blue contours; units: PVU; only values of 1 and
 955 2 PVU are plotted) and its anomalies (shaded; units: PVU); and (c, d) composite
 956 horizontal divergence anomalies (black contours; units: 10^{-6} s^{-1} ; interval: 1; value of
 957 zero is neglected), vertical motion ω (shaded; units: $10^{-2} \text{ Pa s}^{-1}$) anomalies and PV
 958 (blue contours; units: PVU; only values of 1 and 2 PVU are plotted) for high TFI days.
 959 The left and right column are for the vertical-longitudinal cross-section along 39°N
 960 and the vertical-latitude cross-section along 111°E respectively. Black contours in
 961 (a, b) denote the corresponding summer climatology of 1 and 2 PVU surfaces.
 962 Stippled in (a, b) and (c, d) indicate the 90% confidence level of the composite
 963 potential vorticity anomalies and vertical motion anomalies respectively. Areas shaded
 964 in black show the topography.

965

966

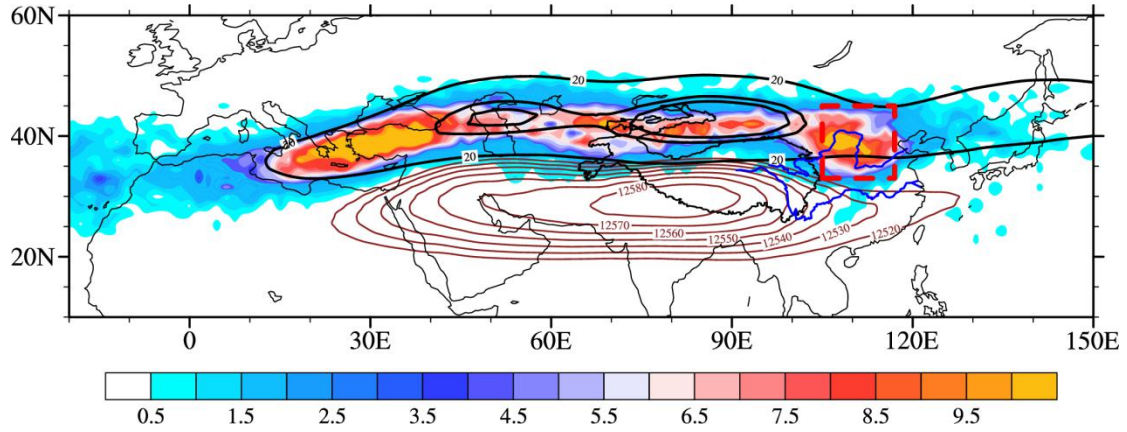
967

968



969

970 **Fig. 3** Composites of (a) PV anomalies (shaded; units: PVU; only those above 90%
 971 confidence level are plotted) and horizontal wind anomalies (vector; units: m s^{-1}) at
 972 300-hPa; (b) horizontal divergence anomalies (shaded; units: 10^{-6} s^{-1}) and horizontal
 973 wind anomalies (vector; units: m s^{-1}) at 700-hPa; (c) rainfall anomalies (shaded; units:
 974 mm) for high TFI days. Stippling areas in (b) and (c) indicate the 90% confidence
 975 level of the composite horizontal divergence anomalies and rainfall anomalies,
 976 respectively. Black arrows in (b) indicate the 90% confidence level of the composite
 977 horizontal wind anomalies.



978

979 **Fig. 4** Composite TF frequency (shaded; units: %), geopotential height (brown
 980 contours; units: gpm; interval: 10; 12520 gpm above) and westerly wind speed (black
 981 contours; units: m s^{-1} ; 20 m s^{-1} above) at 200-hPa for high TFI days. The thin black
 982 solid contour marks the TP's topographic boundary of 1500 m. The blue curves
 983 delineate the Yellow and Yangtze River from north to south.

984

985

986

987

988

989

990

991

992

993

994

995

996

997

998

999

1000

1001

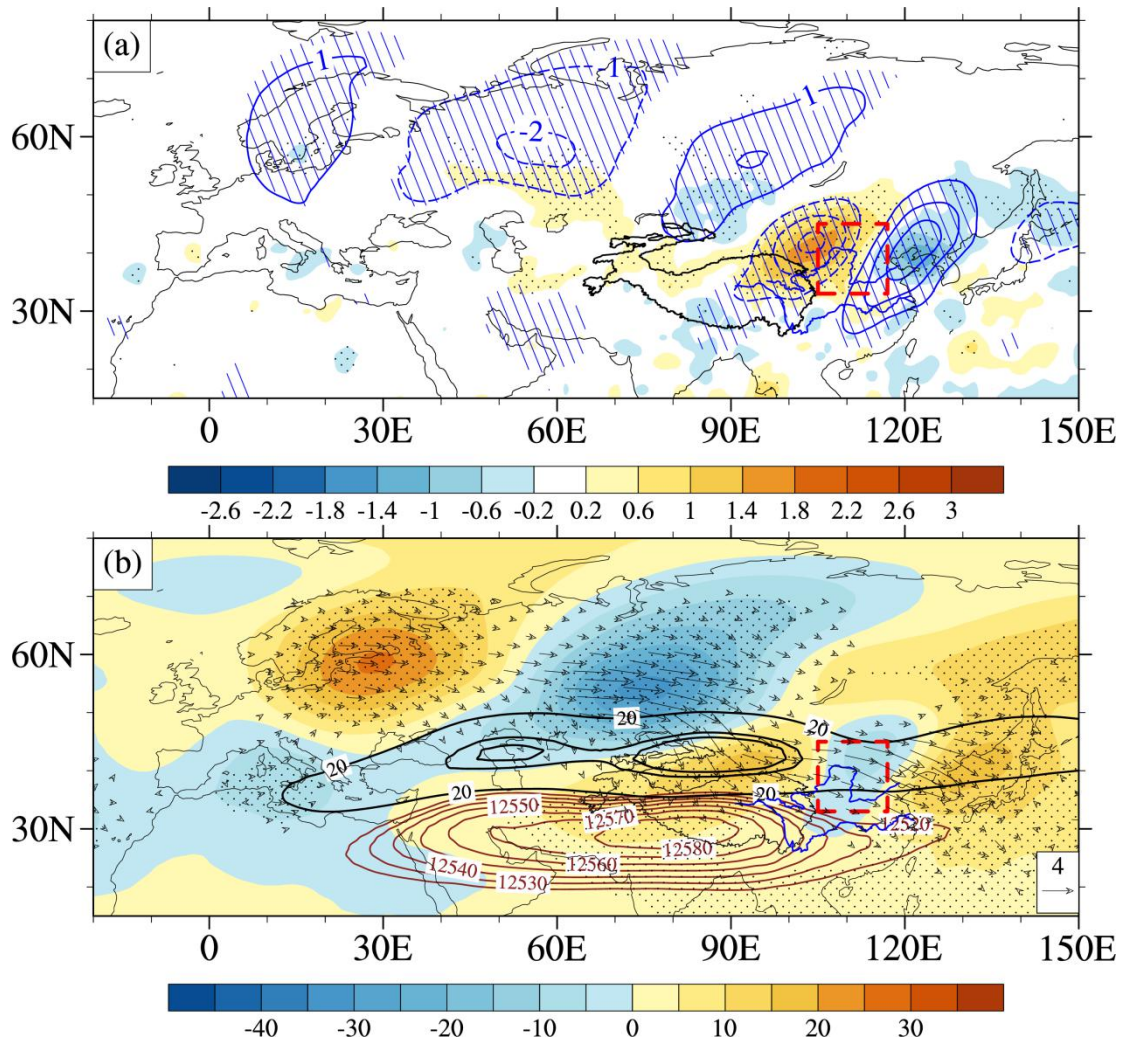
1002

1003

1004

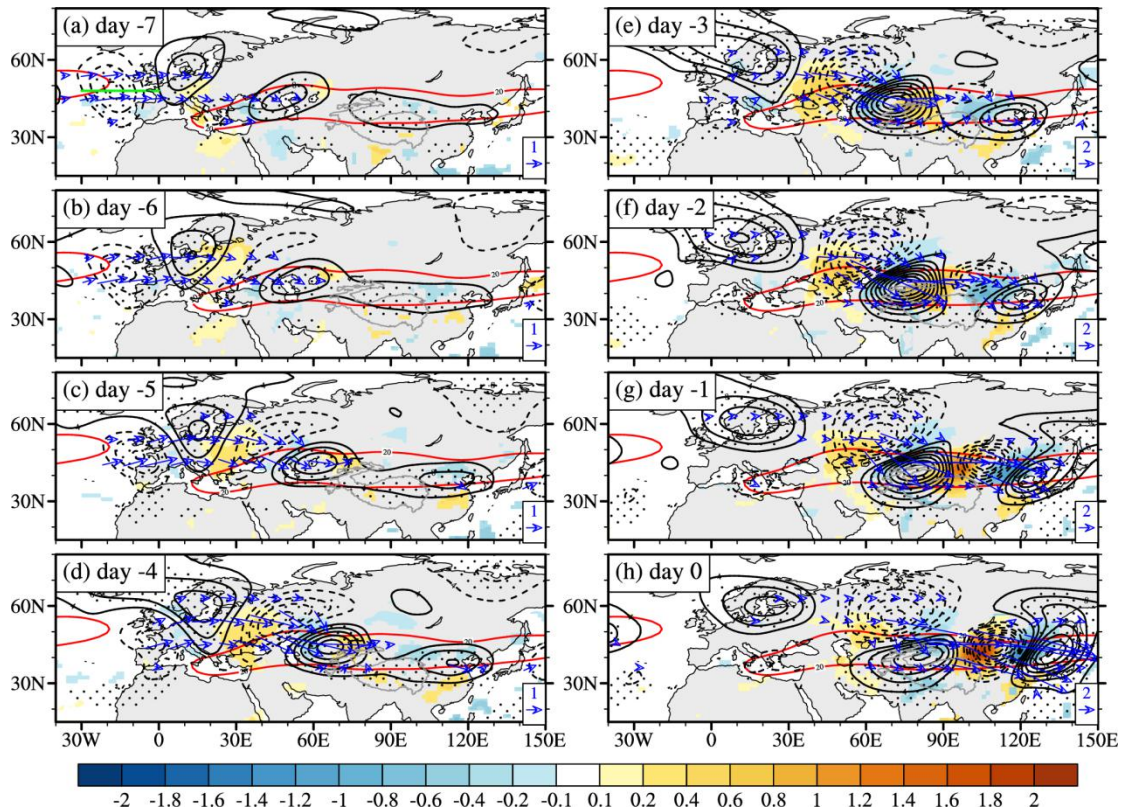
1005

1006



1007
 1008 **Fig. 5** Composite (a) meridional wind (contours; units: m s^{-1} ; interval: 1; Value of zero
 1009 is neglected) and vertical motion ω (shaded; units: $10^{-2} \text{ Pa s}^{-1}$) anomalies at 200-hPa;
 1010 (b) geopotential height (brown contours; units: gpm; interval: 10; 12520 gpm above)
 1011 and its anomalies (shaded; units: gpm), westerly wind speed (black contours; units: m
 1012 s^{-1} ; 20 m s^{-1} above), and wave activity flux (vector; units: $10^{-1} \text{ m}^2 \text{ s}^{-2}$; amplitudes
 1013 larger than 0.05 are shown) anomalies at 200-hPa for high TFI days. The Stippling
 1014 and hatched areas in (a) indicate the 90% confidence level of composite meridional
 1015 wind and vertical motion anomalies, respectively. The Stippling areas in (b) indicate
 1016 the 90% confidence level of the composite geopotential height anomalies.
 1017

1018
 1019
 1020
 1021
 1022
 1023
 1024



1025

1026 **Fig. 6** Lead/lag regressions against the PVI of geopotential height (black contours;
 1027 units: gpm; interval 4; value of zero is ignored), vertical motion ω (shaded; units: 10^{-2}
 1028 Pa s^{-1} ; only the statistical significance at 90% confidence level is plotted), and wave
 1029 activity flux anomalies (vector; units: $10^{-1} \text{ m}^2 \text{ s}^{-2}$; amplitudes larger than 0.5 are shown)

1030 at 200-hPa, when the PVI leads for (a) -7 days, (b) -6 days, (c) -5 days, (d) -4

1031 days, (e) -3 days, (f) -2 days, (g) -1 day, and (h) 0 day. The red contours denote

1032 the westerly jet that is stronger than 20 m s^{-1} at 200-hPa. The stippling areas indicate
 1033 the 90% confidence level of the regressed geopotential height anomalies.

1034

1035

1036

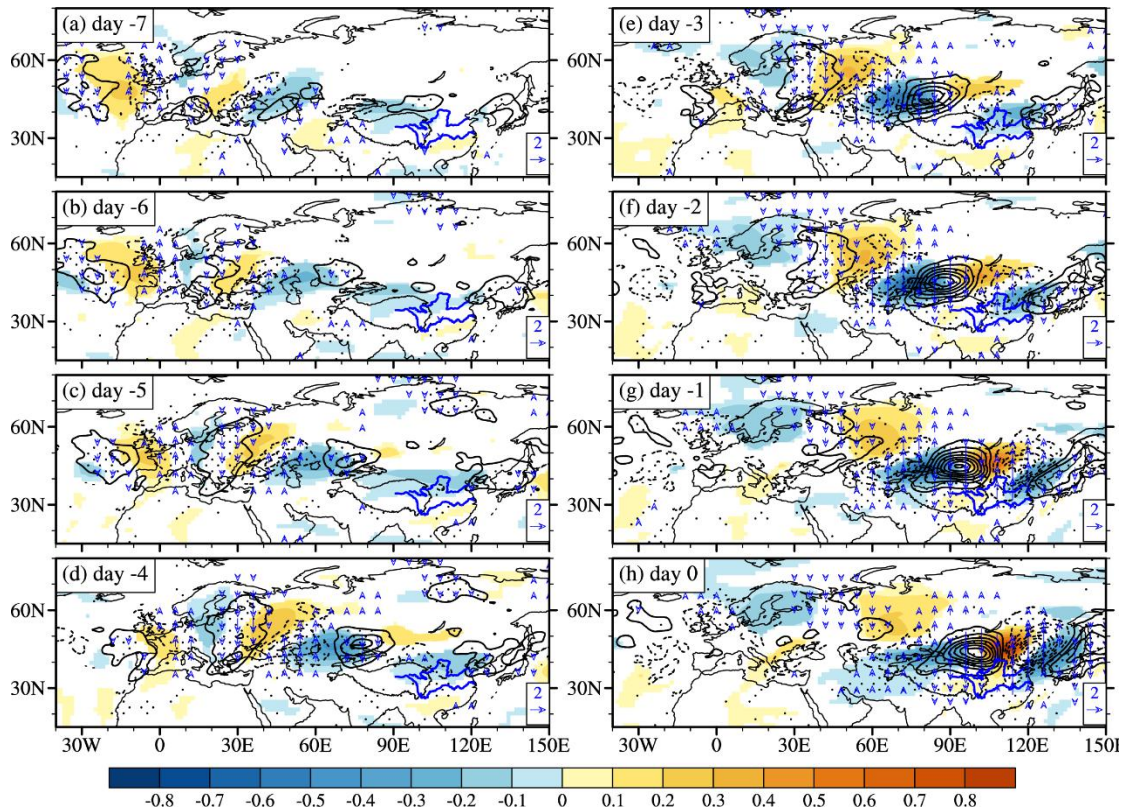
1037

1038

1039

1040

1041



1042

1043 **Fig. 7** As in Fig. 6 but for the PV (shaded; units: PVU; statistical significance at 90%
 1044 confidence level), meridional PV advection (black contours; units: PVU s⁻¹; interval:
 1045 0.4), and meridional wind anomalies (vector; units: m s⁻¹; only the vectors that are
 1046 statistically significant at 95% confidence level are plotted) at 200-hPa. The stippling
 1047 areas indicate the 90% confidence level of the regressed meridional PV advection
 1048 anomalies.

1049

1050

1051

1052

1053

1054

1055

1056

1057

1058

1059

1060

1061

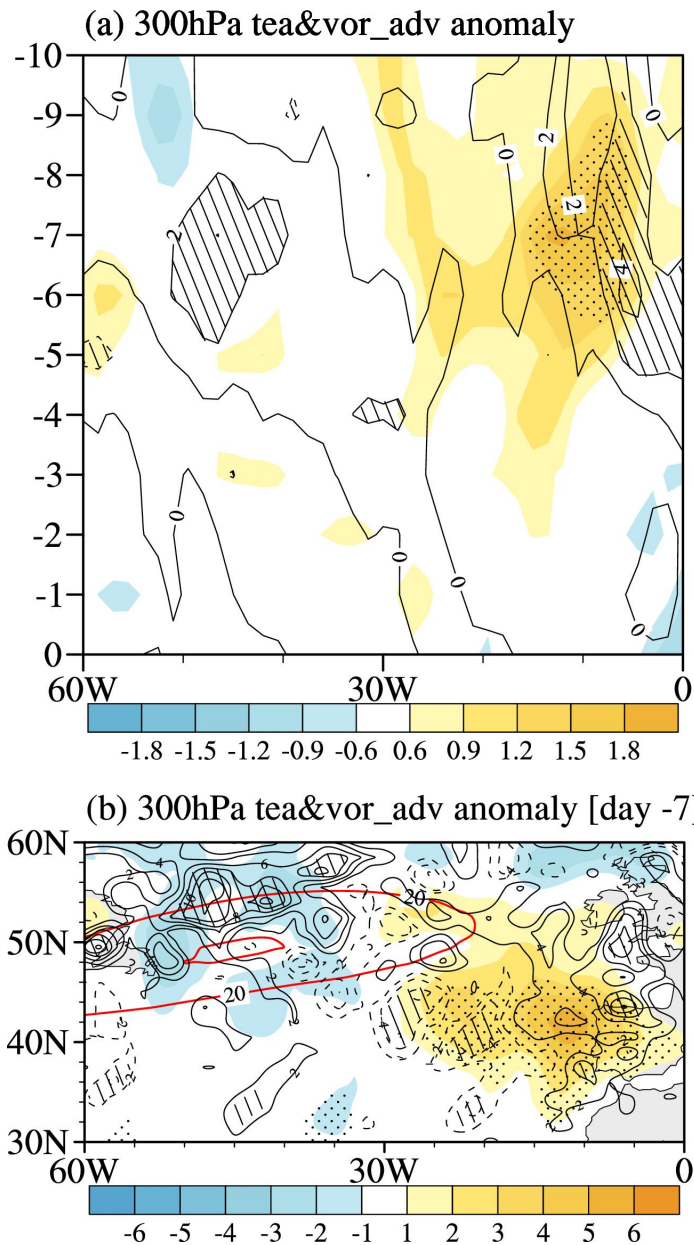
1062

1063

1064

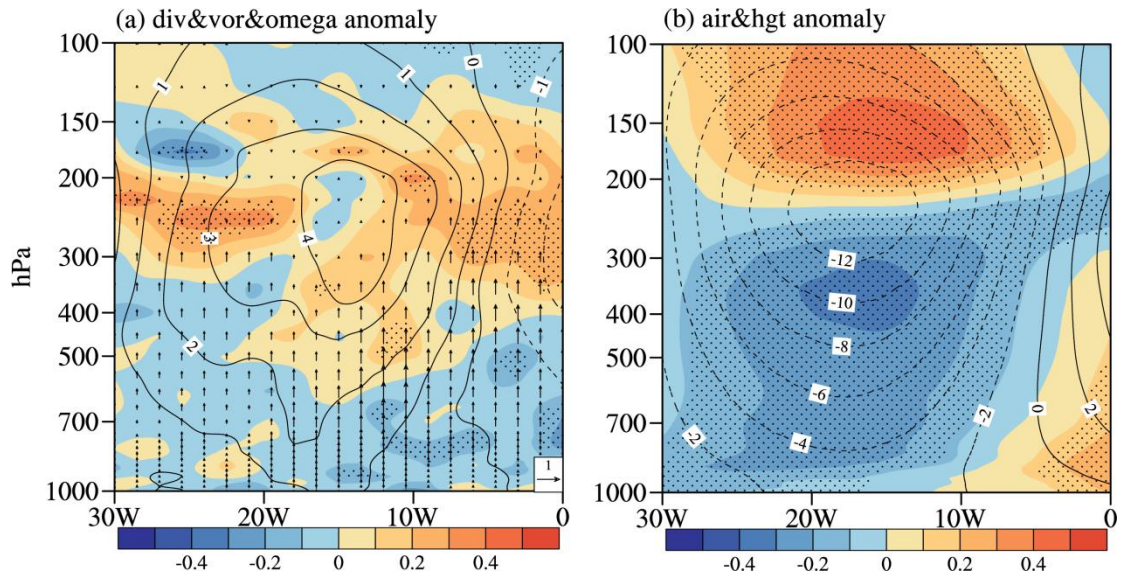
1065

1066



1067
 1068
 1069
 1070
 1071
 1072
 1073
 1074
 1075
 1076
 1077

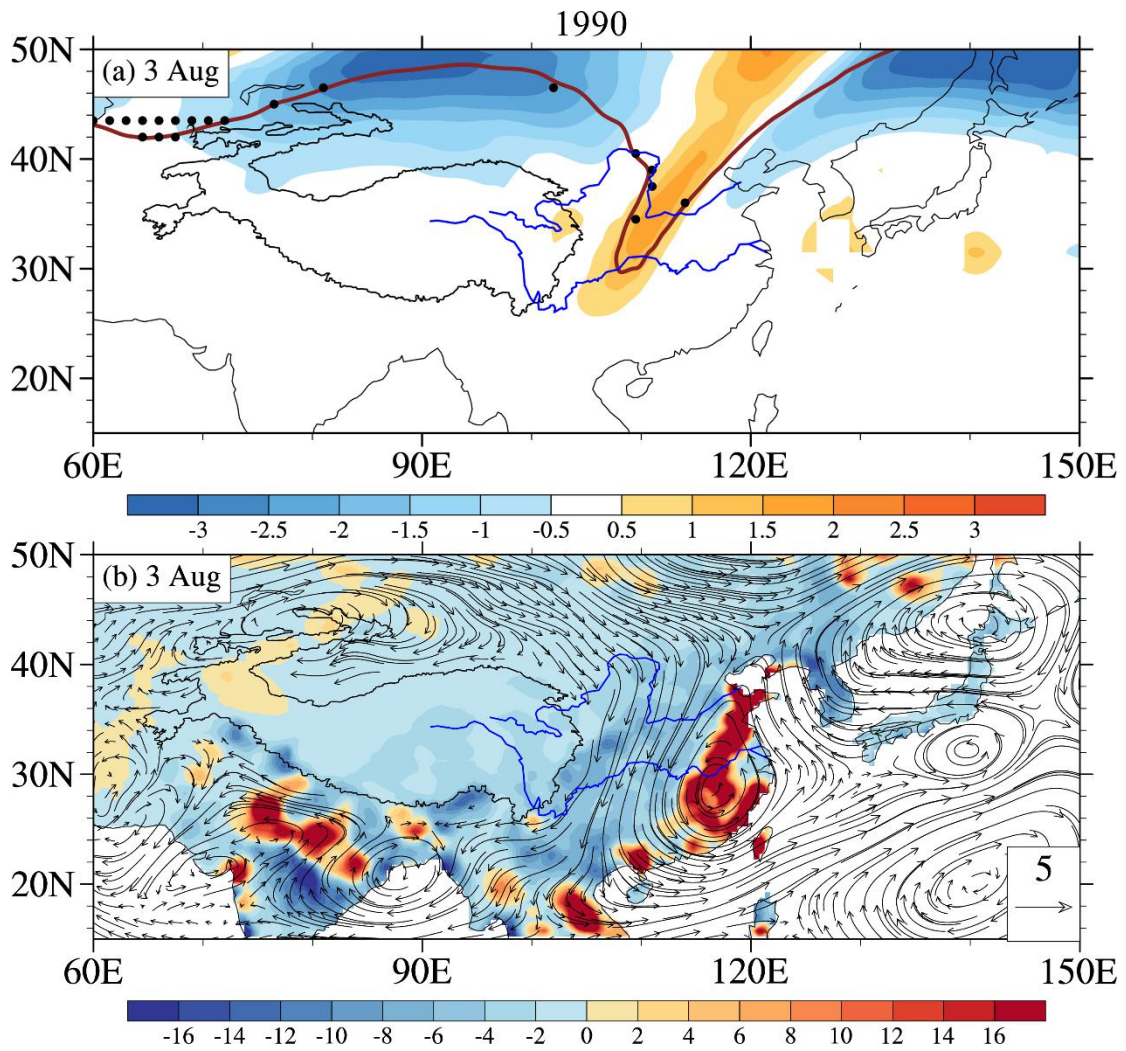
Fig. 8 (a) Temporal evolution of the lead regressions against the PVI from day -10 to day 0 , of transient eddy kinetic energy (shaded; units: $\text{m}^2 \text{s}^{-2}$) and vorticity advection (contours; units: 10^{-6}m s^{-2} ; interval 2) anomalies at 300-hPa along the northern North Atlantic ($32^\circ\text{--}58^\circ\text{N}$); (b) Geographical distribution of the regressed transient eddy kinetic energy (shaded; units: $\text{m}^2 \text{s}^{-2}$) and vorticity advection (contours; units: 10^{-6}m s^{-2} ; interval 2 ; value of zero is ignored) anomalies at 300-hPa at day -7 . The red contours denote the westerly jet (units: m s^{-1} ; interval: 4 ; values above 20 are plotted) at 300-hPa . Stipplings and slashes in (a) and (b) indicate the 90% confidence level of the regressions respectively for the transient eddy kinetic energy and vorticity advection anomalies.



1078

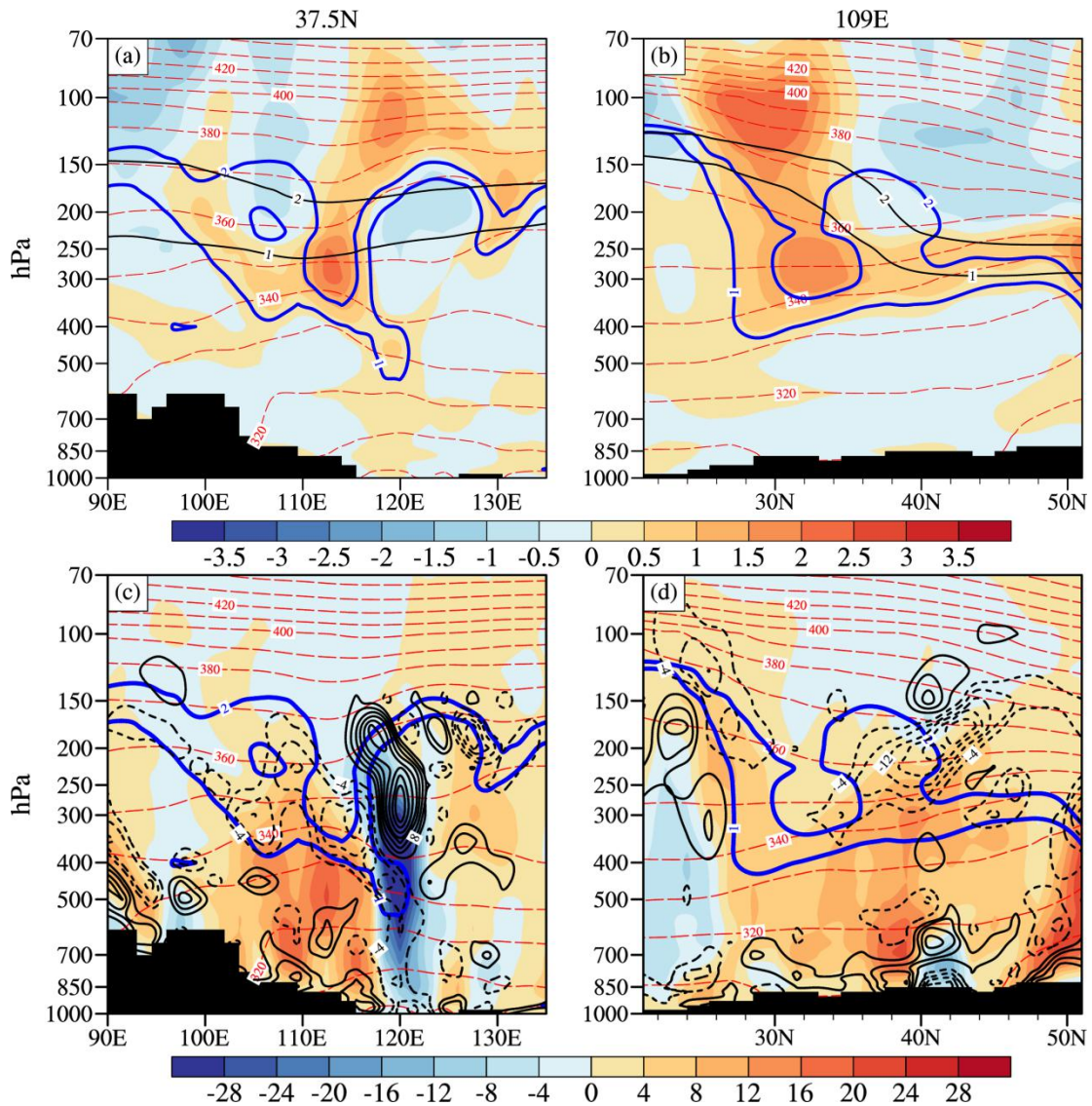
1079 **Fig. 9** Vertical cross sections of (a) the regressed horizontal divergence (shaded; units:
 1080 10^{-6} s^{-1}), relative vorticity (contours; units: 10^{-6} s^{-1}), and vertical motion ω anomalies
 1081 (vectors; units: $10^{-3} \text{ Pa s}^{-1}$); and (b) the regressed air temperature (shaded; units: $^{\circ}\text{C}$),
 1082 and geopotential height (contours; units: gpm) anomalies against the PVI along 48°N
 1083 over the northern North Atlantic at day -7 . Stipplings indicate the 90% confidence
 1084 level of the regression for (a) the horizontal divergence anomalies and (b) the air
 1085 temperature anomalies, respectively. The ordinate in (a, b) is the pressure level (units:
 1086 hPa).

1087

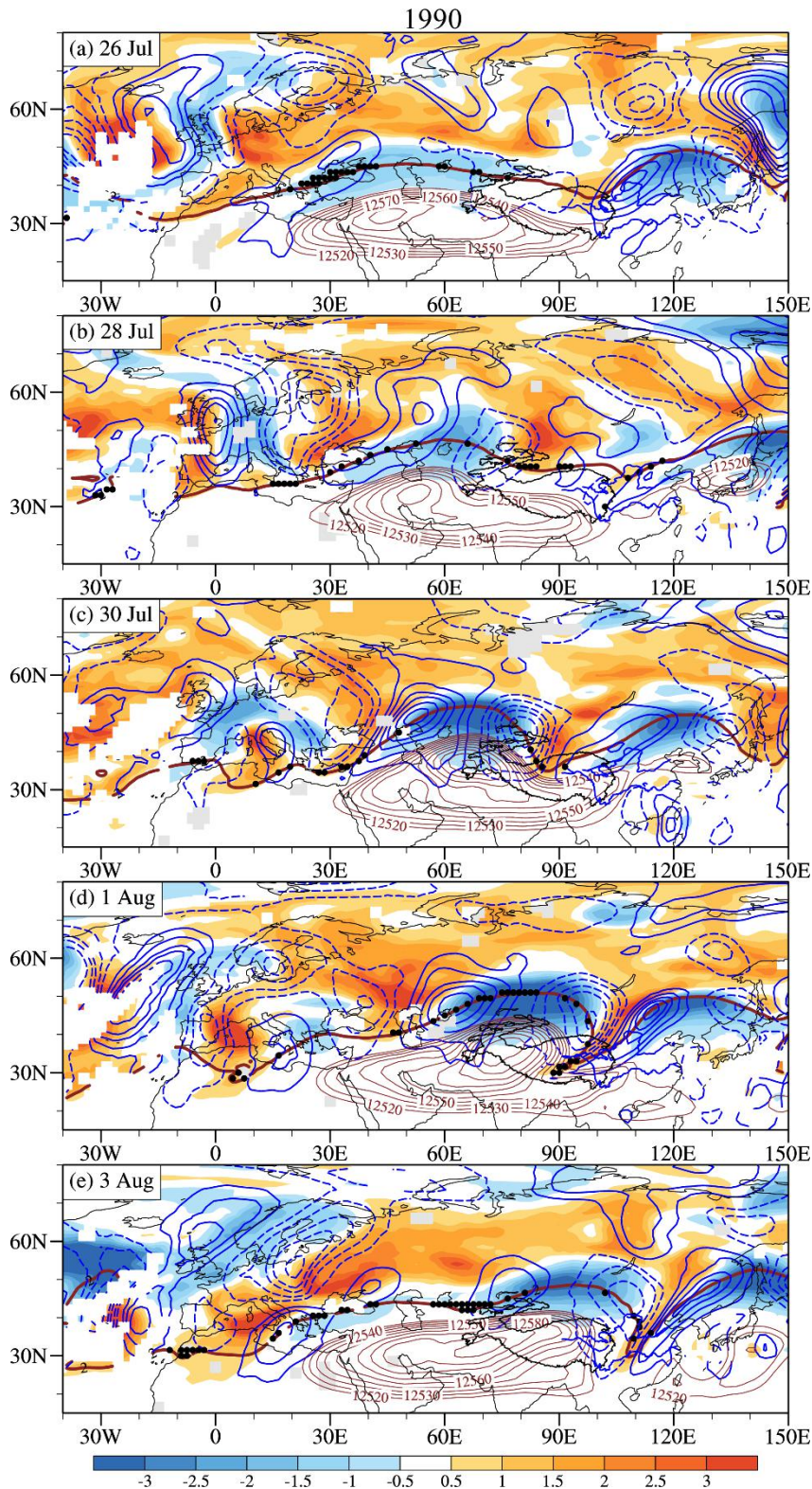


1088
 1089 **Fig. 10** Distribution of (a) the tropopause (2 PVU contour, bold brown), PV anomalies
 1090 (shaded; units: PVU) on 350K isentropic surface, and (b) horizontal wind anomalies
 1091 (vector; units: m s^{-1}) at 700-hPa and precipitation anomalies (shaded; units: mm d^{-1})
 1092 on 3 August, 1990.

1093
 1094
 1095
 1096
 1097
 1098
 1099
 1100
 1101
 1102
 1103
 1104
 1105
 1106
 1107

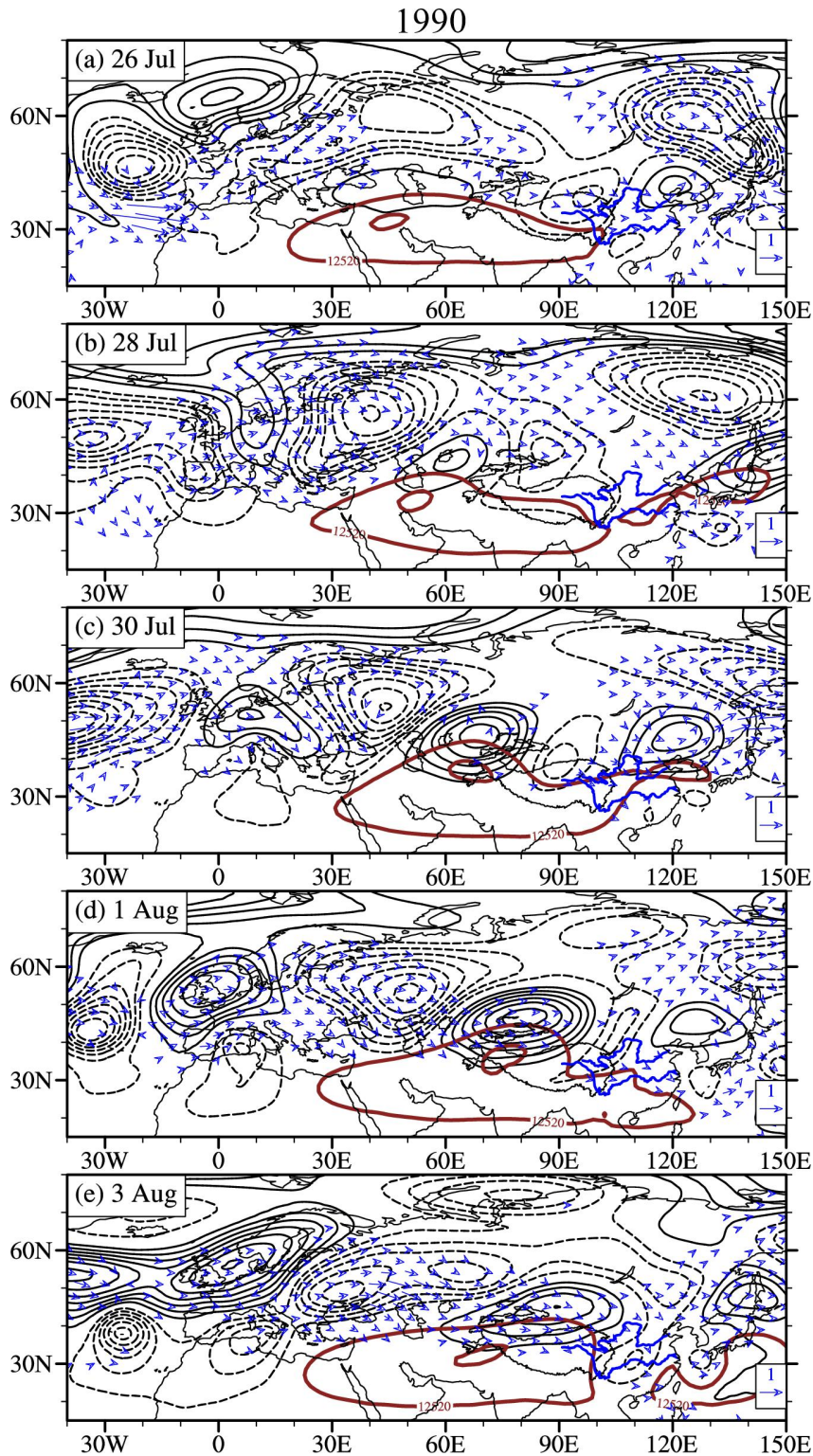


1108
 1109 **Fig. 11** Vertical cross sections of (a, b) potential temperature (red dashed contours;
 1110 units: K; interval: 10), PV (blue contours; units: PVU; only values of 1 and 2 PVU are
 1111 plotted) and its anomalies (shaded; units: PVU) on 3 August, 1990; and (c, d)
 1112 horizontal divergence anomalies (black contours; units: 10^{-6} s^{-1} ; interval: 4; value of
 1113 zero is neglected), vertical motion ω (shaded; units: $10^{-2} \text{ Pa s}^{-1}$) anomalies and PV
 1114 (blue contours; units: PVU; only values of 1 and 2 PVU are plotted) on 3 August,
 1115 1990. The left and right column are for the vertical-longitudinal cross-section along
 1116 37.5°N and the vertical-latitudinal cross-section along 109°E respectively. Black
 1117 contours in (a,b) are the corresponding summer climatology of 1 and 2 PVU. Areas
 1118 shaded in black show the topography.
 1119



1120

1121 **Fig. 12** Distribution of PV (shaded; units: PVU), the tropopause (2 PVU contour, bold
 1122 brown) and the meridional wind anomalies (blue contours; units: m s^{-1} ; interval: 6;
 1123 value of zero is neglected) at 350K isentropic surface, black dots mark the locations
 1124 where tropopause folding occurred; And geopotential height at 200 hPa (red contours;
 1125 units: gpm; interval: 10; above 12520 gpm) on (a) 26 July, (b) 28 July, (c) 30 July, (d)
 1126 1 August and (e) 3 August, 1990, respectively.



1127

1128 **Fig. 13** Spatial distribution of geopotential height (brown contours; units: gpm) and
 1129 its anomalies (black contours; units: gpm; interval: 10; value of zero is neglected), and
 1130 wave activity flux (vector; units: $10^2 \text{ m}^2 \text{ s}^{-2}$; amplitudes larger than 8 are shown) on (a)
 1131 26 July, (b) 28 July, (c) 30 July, (d) 1 August and (e) 3 August, 1990, respectively.

1132

1133

Figures

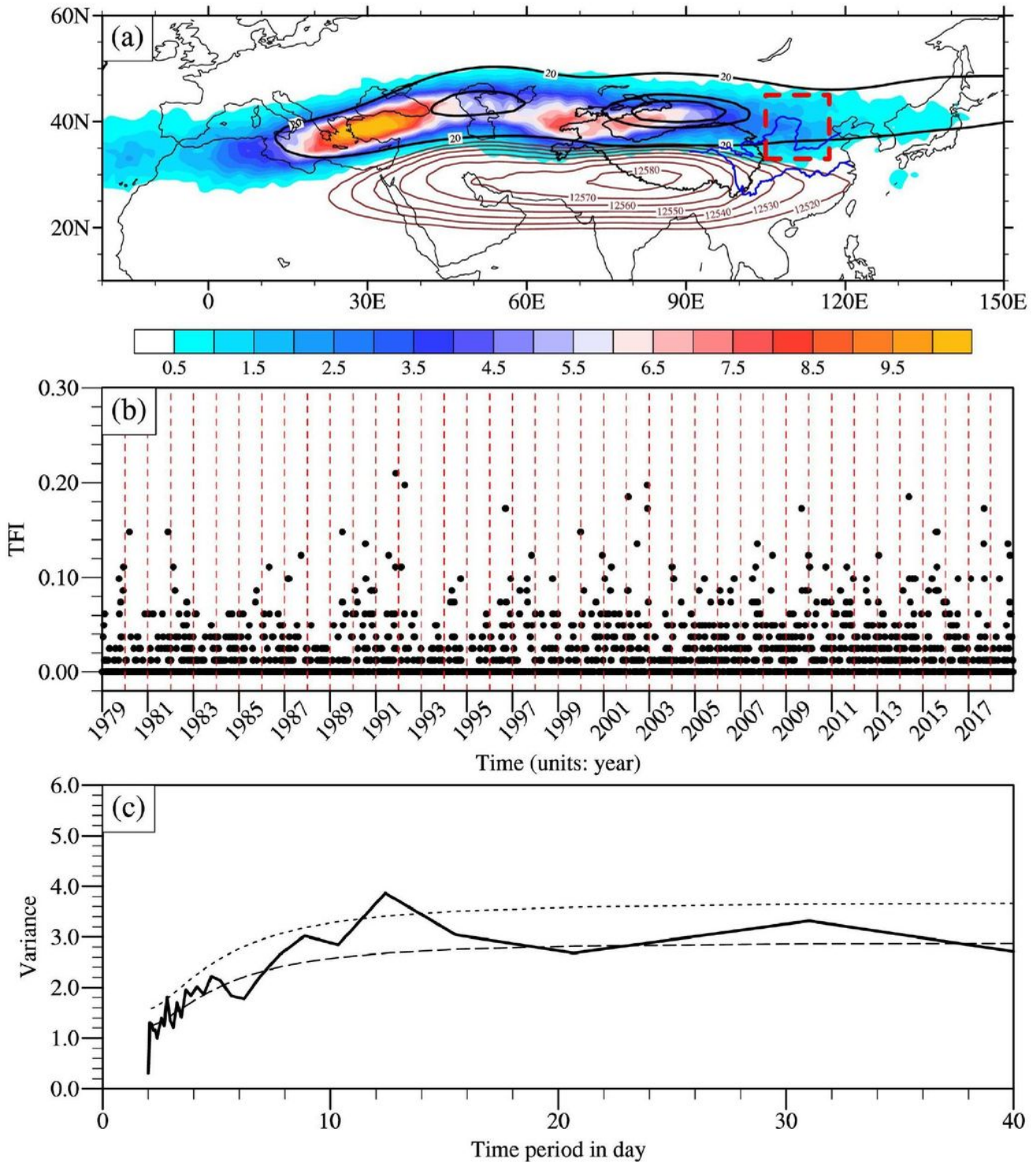


Figure 1

Please see the Manuscript PDF file for the complete figure caption Note: The designations employed and the presentation of the material on this map do not imply the expression of any opinion whatsoever on the part of Research Square concerning the legal status of any country, territory, city or area or of its

authorities, or concerning the delimitation of its frontiers or boundaries. This map has been provided by the authors.

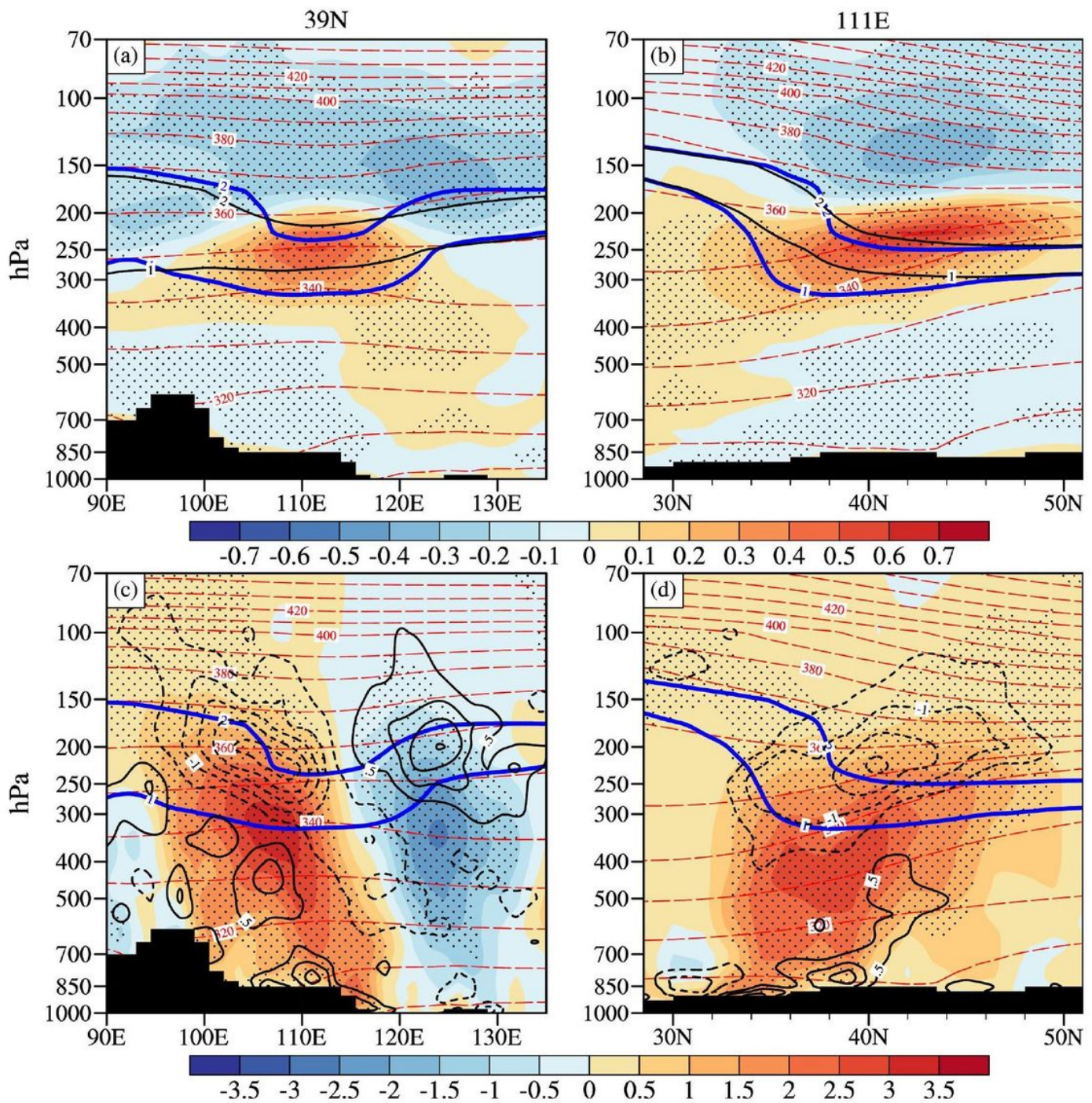


Figure 2

Please see the Manuscript PDF file for the complete figure caption Note: The designations employed and the presentation of the material on this map do not imply the expression of any opinion whatsoever on the part of Research Square concerning the legal status of any country, territory, city or area or of its authorities, or concerning the delimitation of its frontiers or boundaries. This map has been provided by the authors.

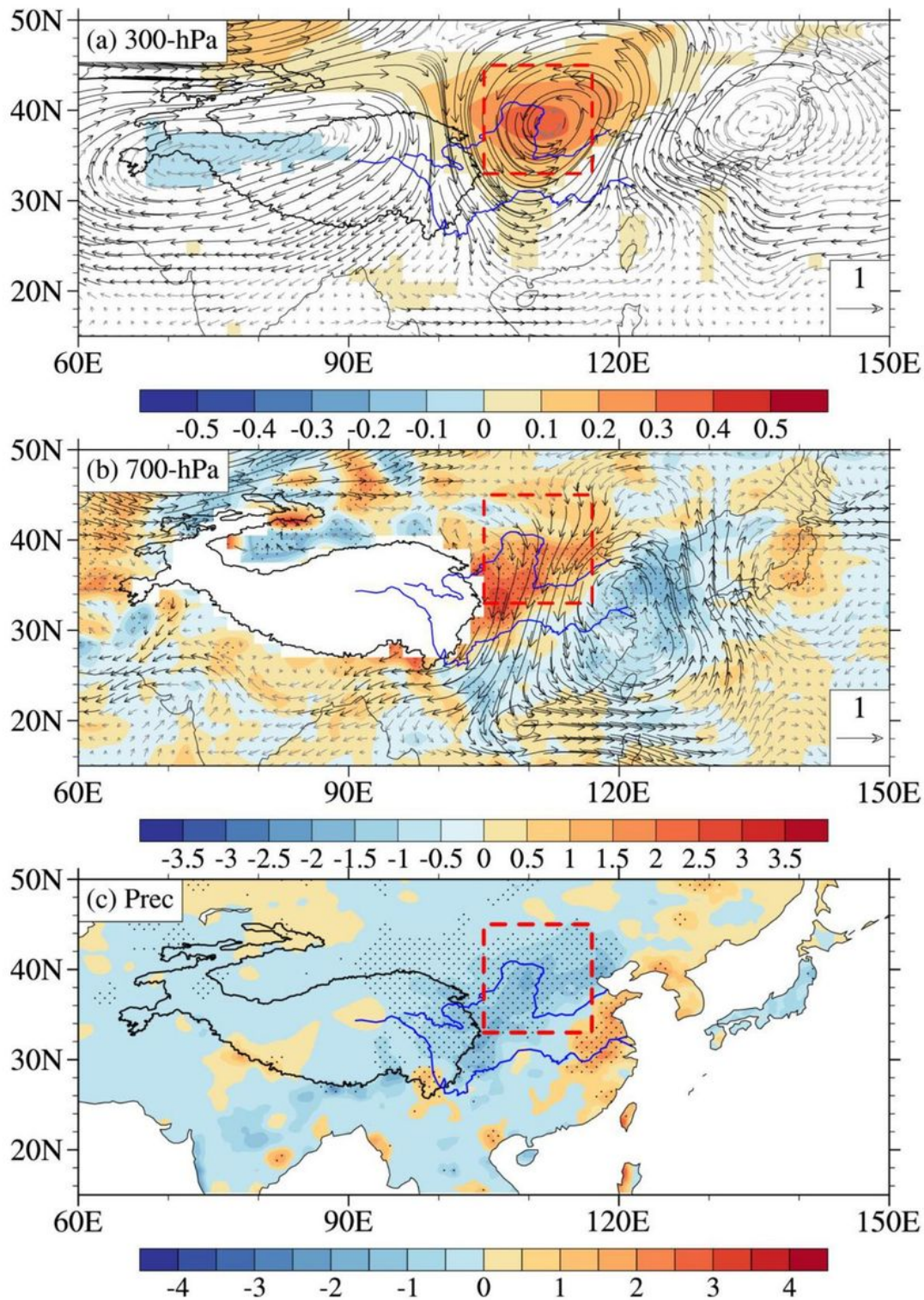


Figure 3

Please see the Manuscript PDF file for the complete figure caption Note: The designations employed and the presentation of the material on this map do not imply the expression of any opinion whatsoever on the part of Research Square concerning the legal status of any country, territory, city or area or of its authorities, or concerning the delimitation of its frontiers or boundaries. This map has been provided by the authors.

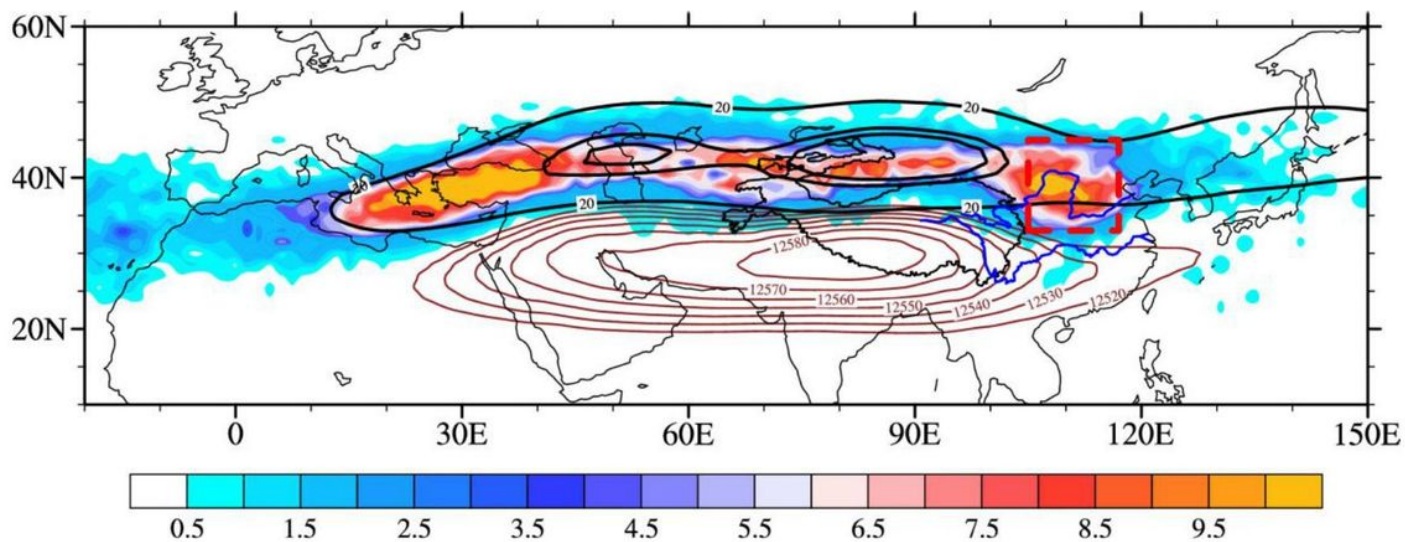


Figure 4

Please see the Manuscript PDF file for the complete figure caption Note: The designations employed and the presentation of the material on this map do not imply the expression of any opinion whatsoever on the part of Research Square concerning the legal status of any country, territory, city or area or of its authorities, or concerning the delimitation of its frontiers or boundaries. This map has been provided by the authors.

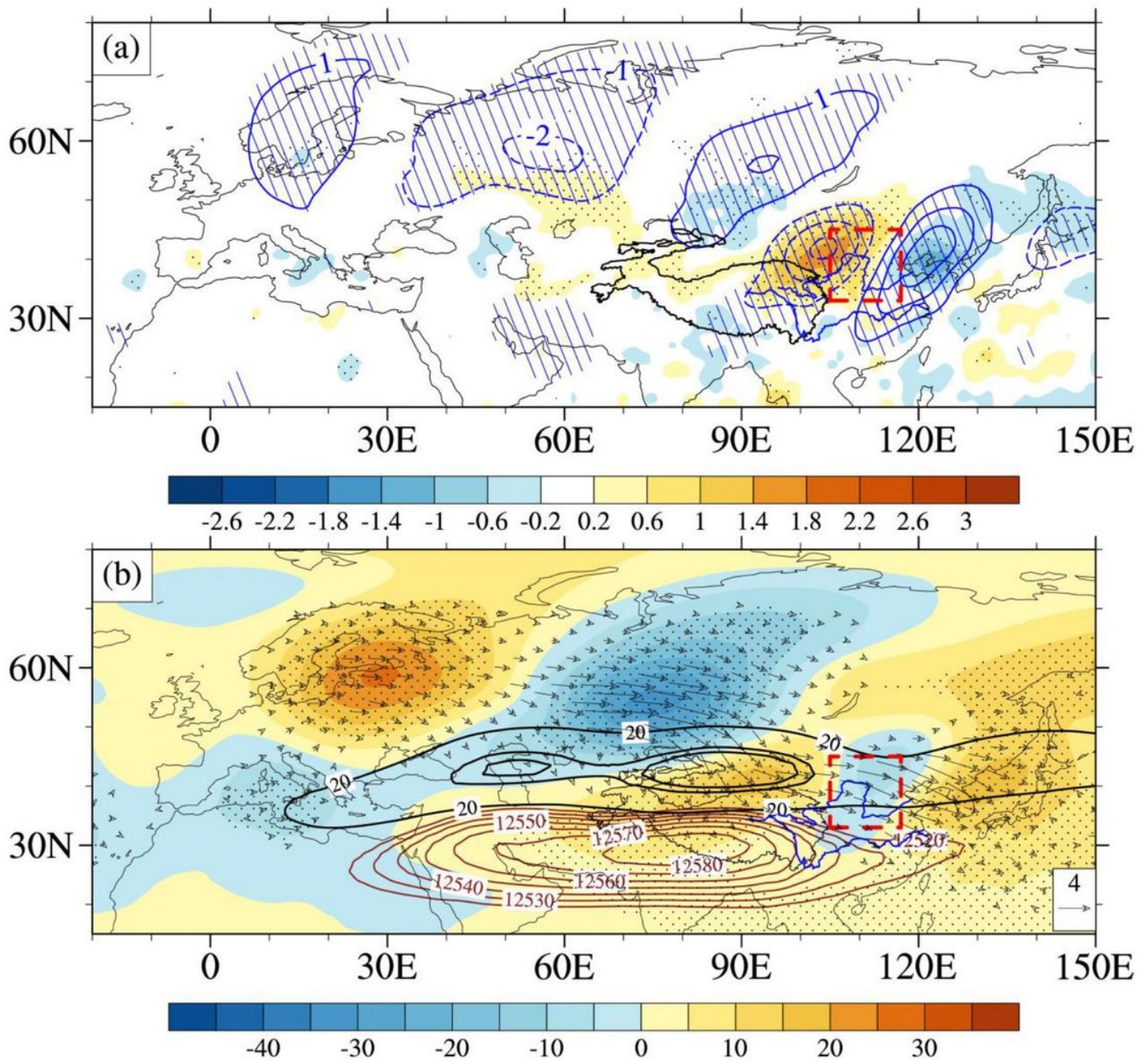


Figure 5

Please see the Manuscript PDF file for the complete figure caption Note: The designations employed and the presentation of the material on this map do not imply the expression of any opinion whatsoever on the part of Research Square concerning the legal status of any country, territory, city or area or of its authorities, or concerning the delimitation of its frontiers or boundaries. This map has been provided by the authors.

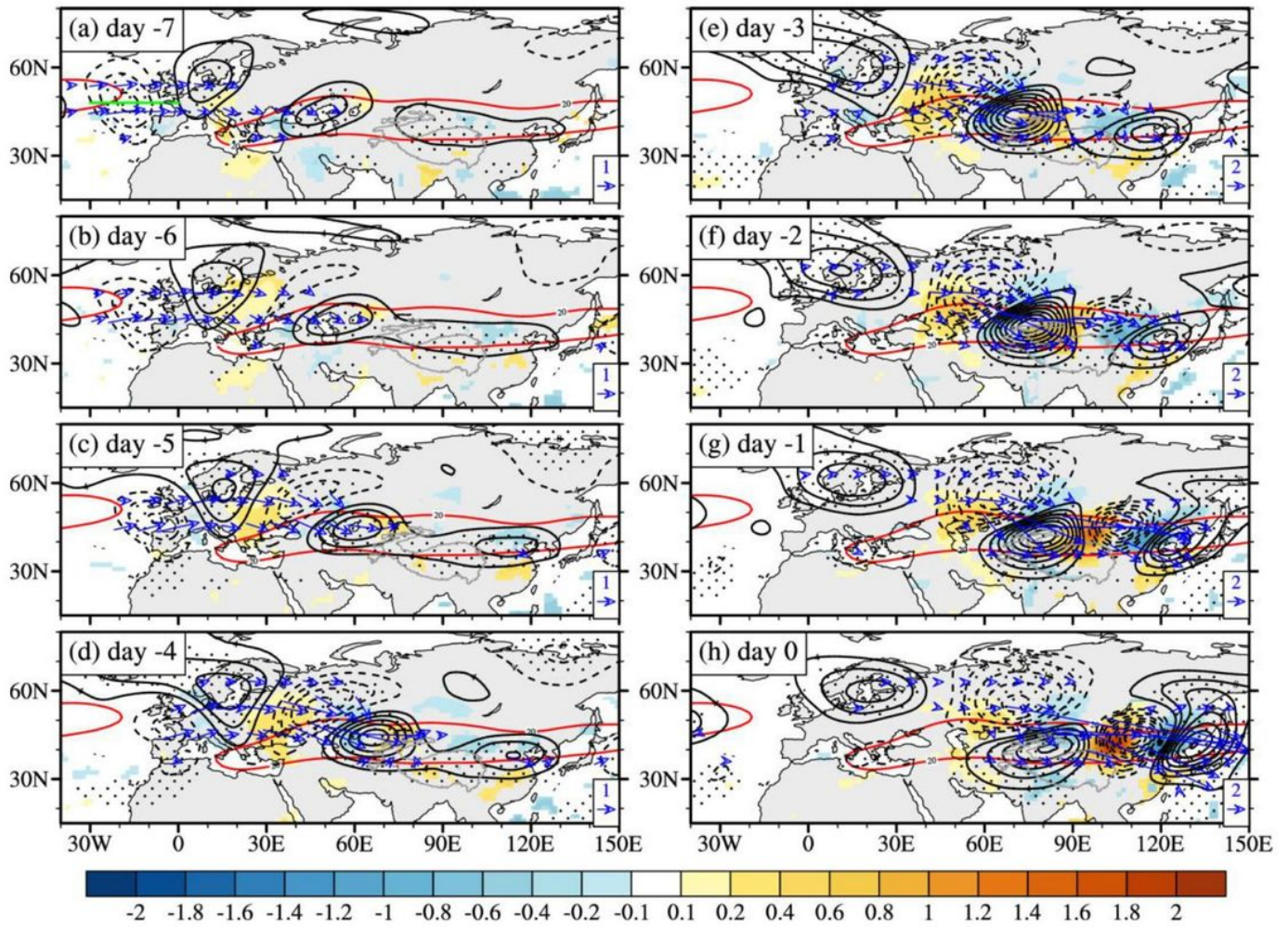


Figure 6

Please see the Manuscript PDF file for the complete figure caption Note: The designations employed and the presentation of the material on this map do not imply the expression of any opinion whatsoever on the part of Research Square concerning the legal status of any country, territory, city or area or of its authorities, or concerning the delimitation of its frontiers or boundaries. This map has been provided by the authors.

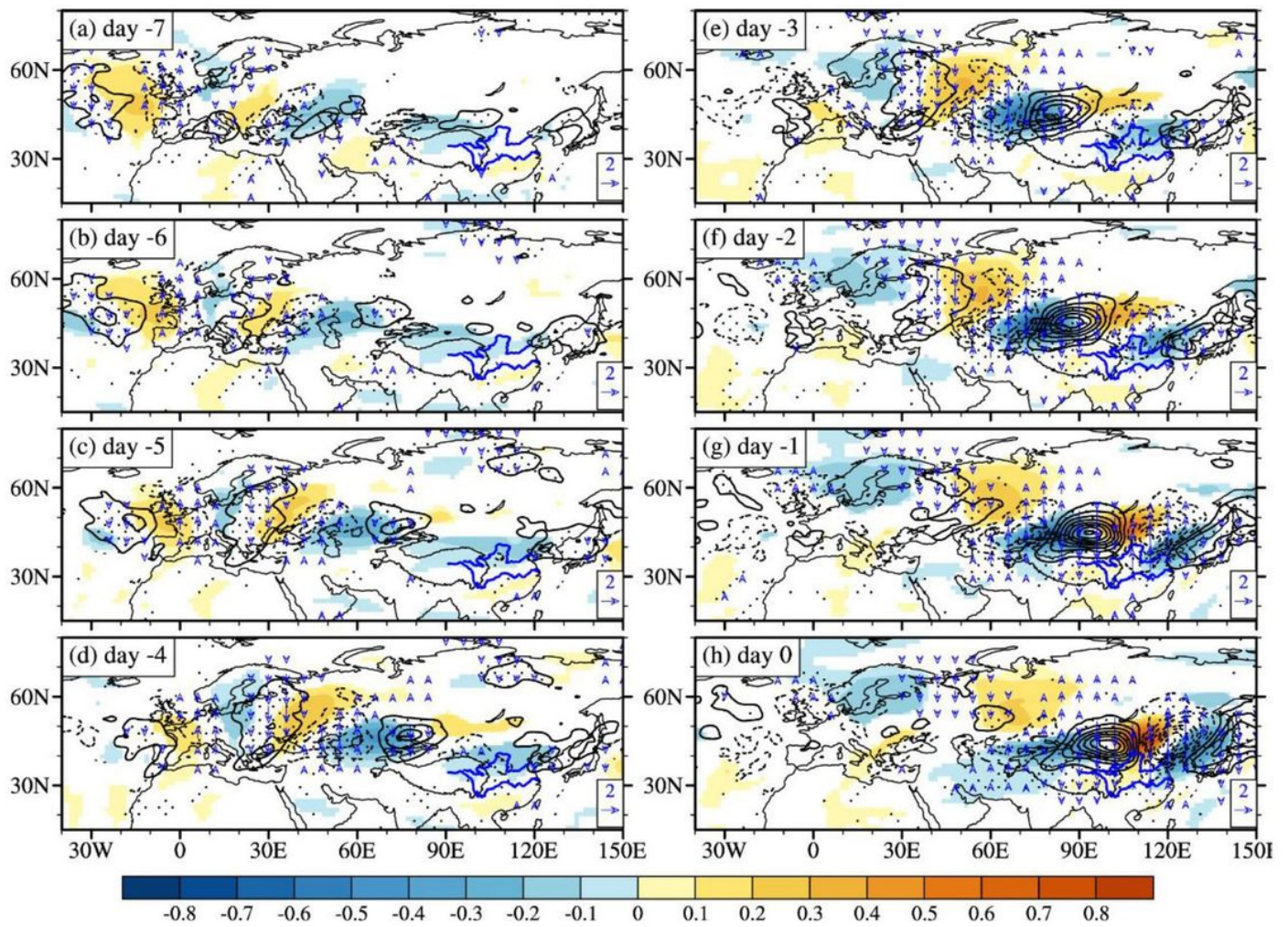


Figure 7

Please see the Manuscript PDF file for the complete figure caption Note: The designations employed and the presentation of the material on this map do not imply the expression of any opinion whatsoever on the part of Research Square concerning the legal status of any country, territory, city or area or of its authorities, or concerning the delimitation of its frontiers or boundaries. This map has been provided by the authors.

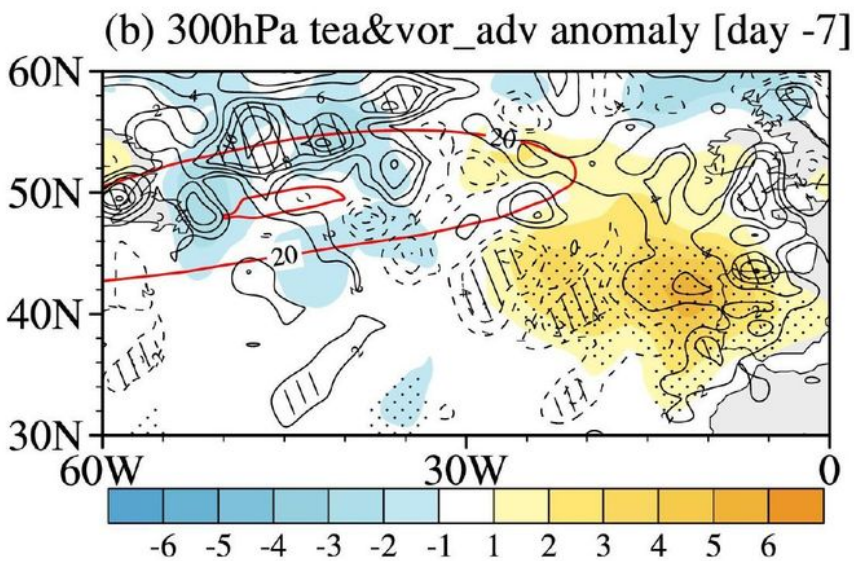
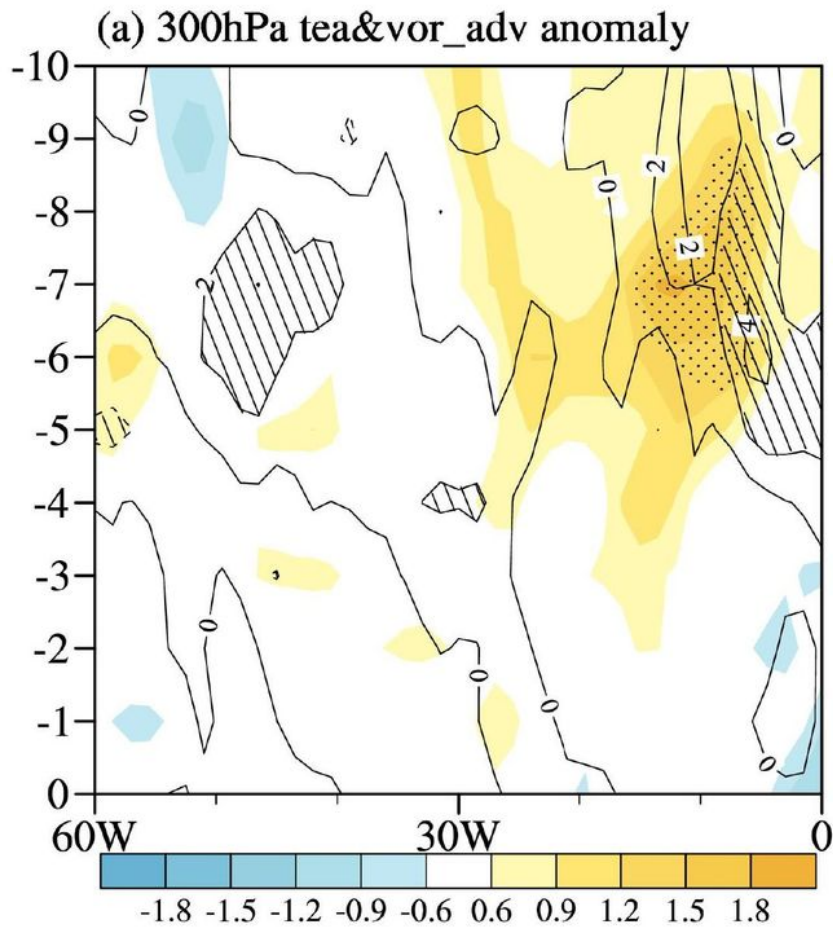


Figure 8

Please see the Manuscript PDF file for the complete figure caption Note: The designations employed and the presentation of the material on this map do not imply the expression of any opinion whatsoever on the part of Research Square concerning the legal status of any country, territory, city or area or of its authorities, or concerning the delimitation of its frontiers or boundaries. This map has been provided by the authors.

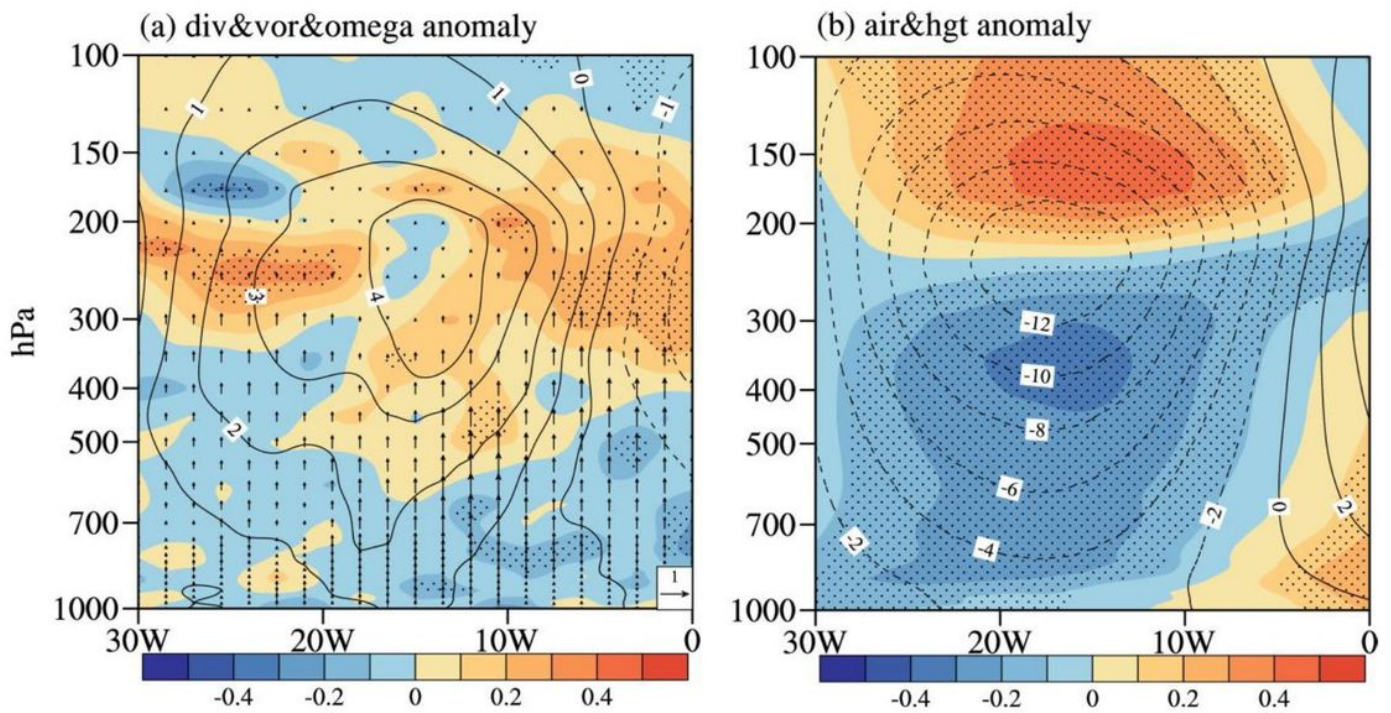


Figure 9

Please see the Manuscript PDF file for the complete figure caption Note: The designations employed and the presentation of the material on this map do not imply the expression of any opinion whatsoever on the part of Research Square concerning the legal status of any country, territory, city or area or of its authorities, or concerning the delimitation of its frontiers or boundaries. This map has been provided by the authors.

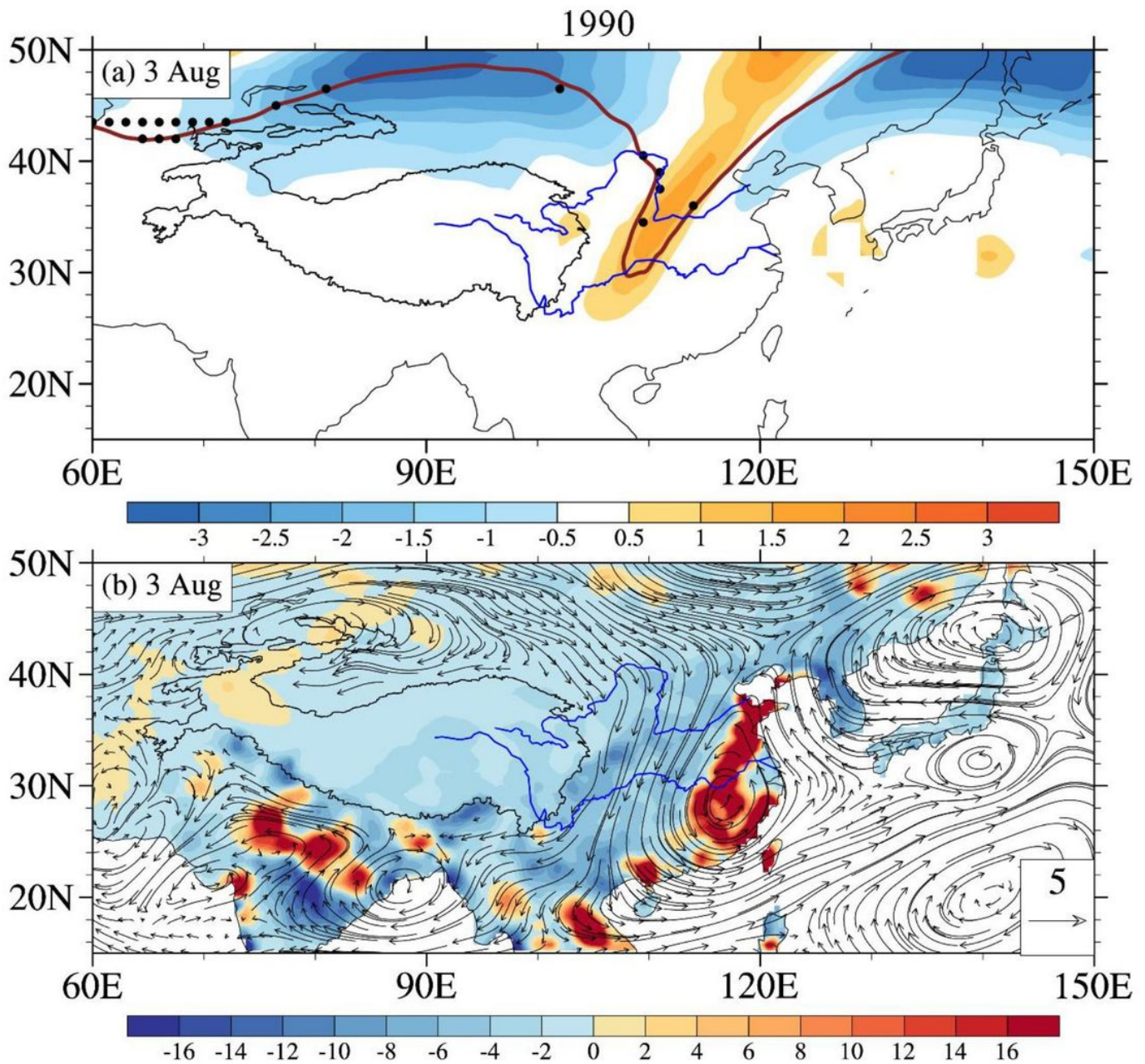


Figure 10

Please see the Manuscript PDF file for the complete figure caption Note: The designations employed and the presentation of the material on this map do not imply the expression of any opinion whatsoever on the part of Research Square concerning the legal status of any country, territory, city or area or of its authorities, or concerning the delimitation of its frontiers or boundaries. This map has been provided by the authors.

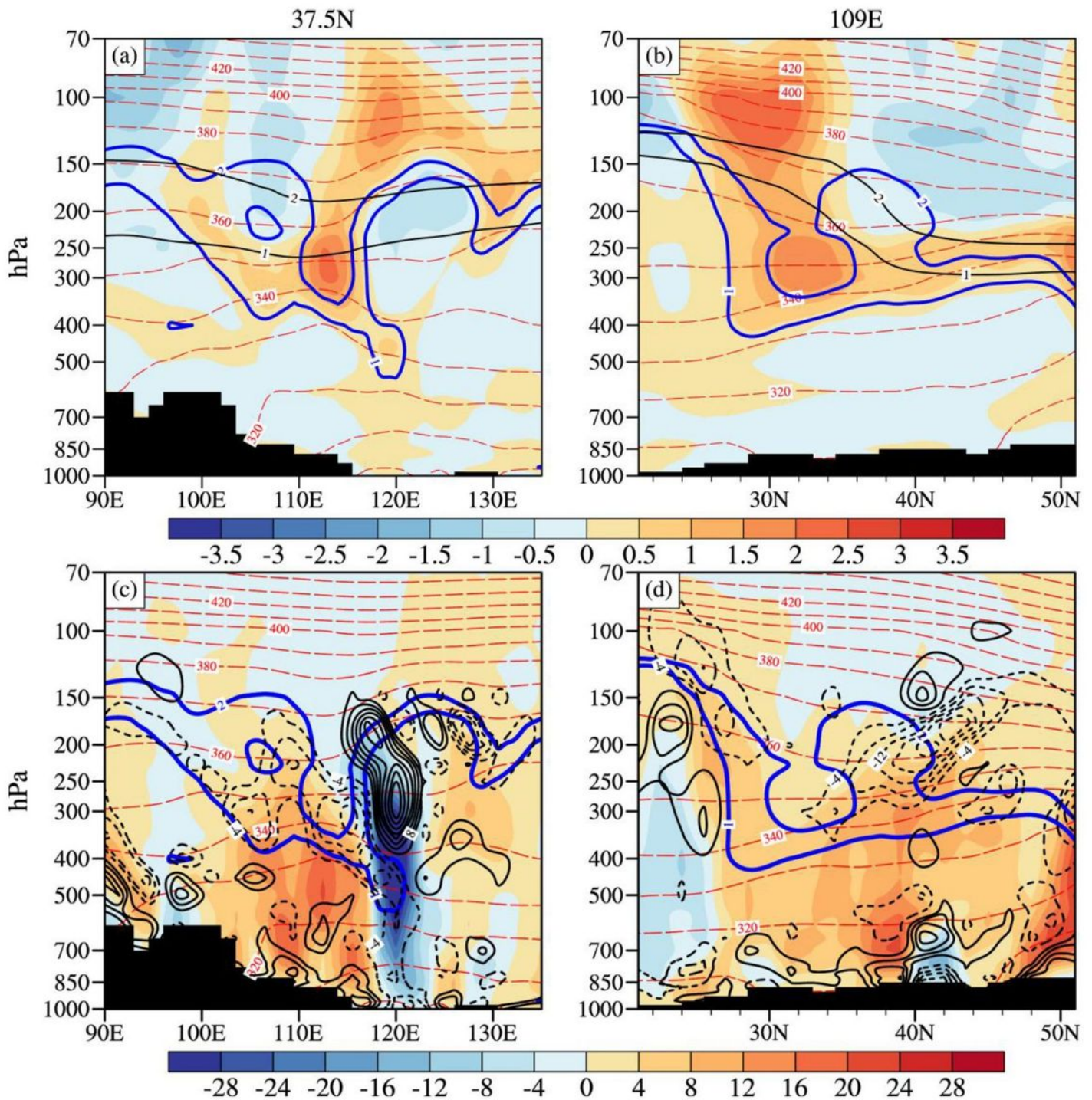


Figure 11

Please see the Manuscript PDF file for the complete figure caption Note: The designations employed and the presentation of the material on this map do not imply the expression of any opinion whatsoever on the part of Research Square concerning the legal status of any country, territory, city or area or of its authorities, or concerning the delimitation of its frontiers or boundaries. This map has been provided by the authors.

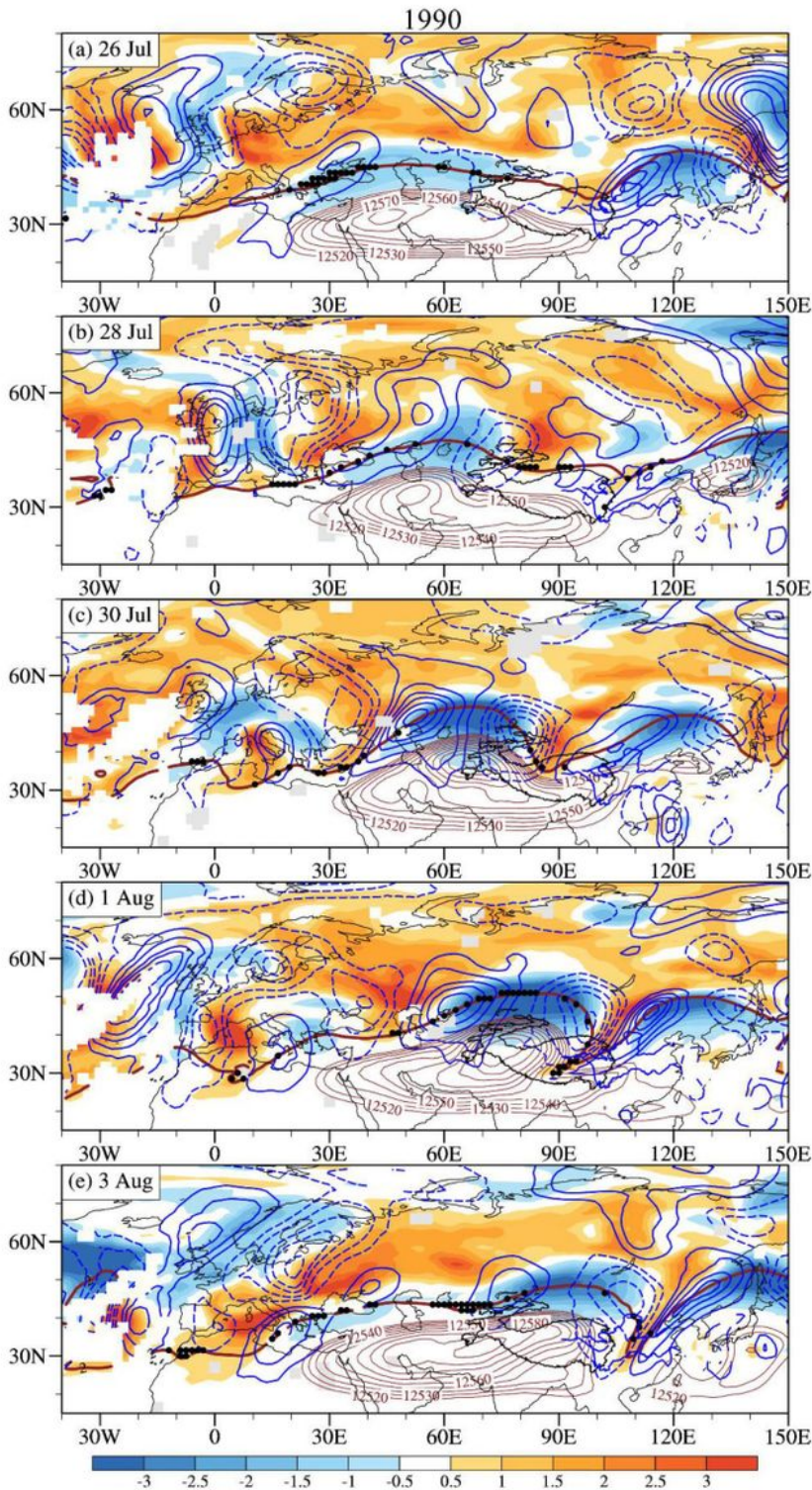


Figure 12

Please see the Manuscript PDF file for the complete figure caption Note: The designations employed and the presentation of the material on this map do not imply the expression of any opinion whatsoever on the part of Research Square concerning the legal status of any country, territory, city or area or of its authorities, or concerning the delimitation of its frontiers or boundaries. This map has been provided by the authors.

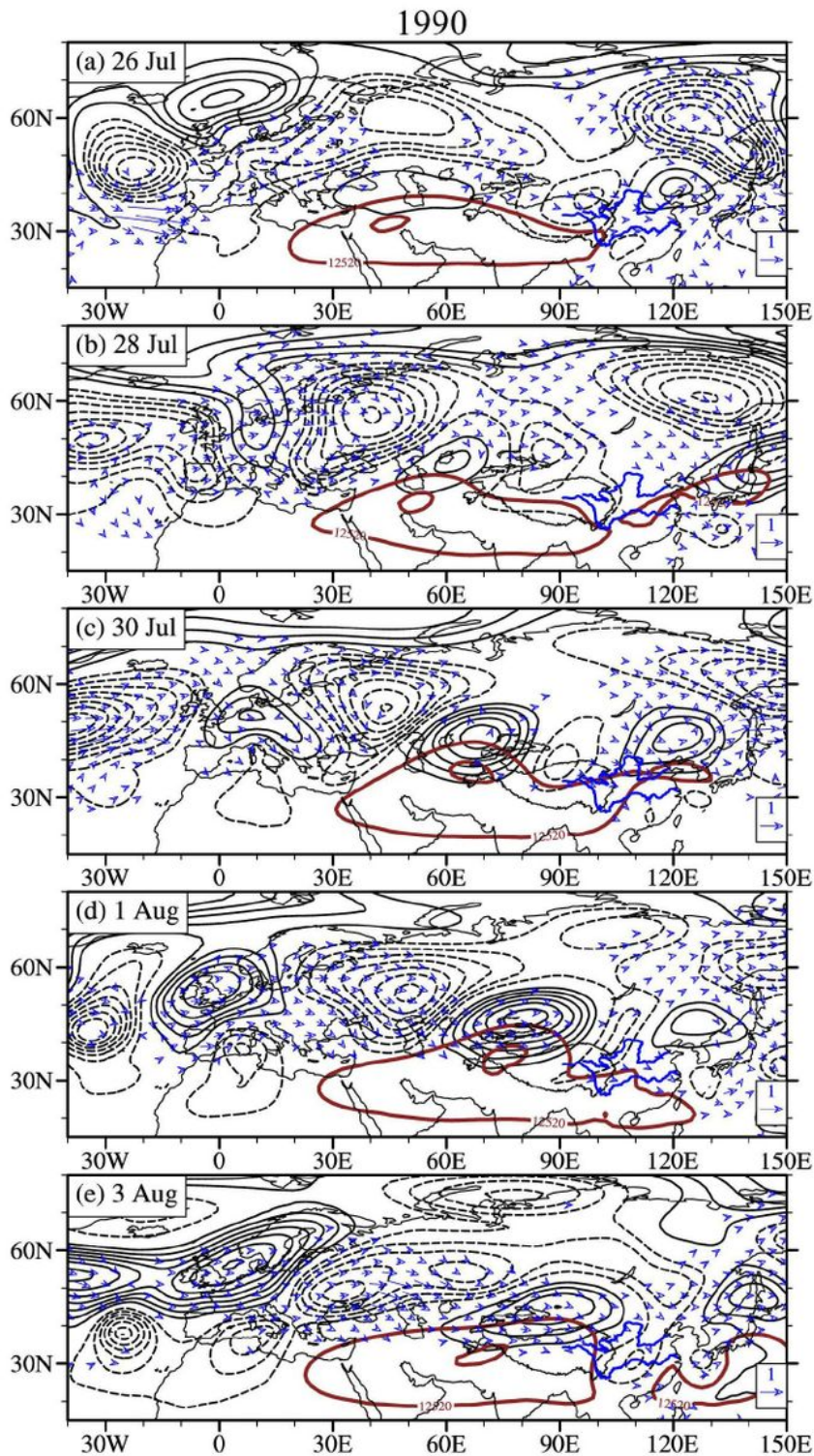


Figure 13

Please see the Manuscript PDF file for the complete figure caption Note: The designations employed and the presentation of the material on this map do not imply the expression of any opinion whatsoever on the part of Research Square concerning the legal status of any country, territory, city or area or of its authorities, or concerning the delimitation of its frontiers or boundaries. This map has been provided by the authors.